Journal of Computational Physics 228 (2009) 2391–2425

Contents lists available at ScienceDirect

Journal of Computational Physics

journal homepage: www.elsevier.com/locate/jcp

A high-order cell-centered Lagrangian scheme for two-dimensional compressible fluid flows on unstructured meshes

Pierre-Henri Maire

UMR CELIA, Université Bordeaux I, 351 Cours de la Libération, 33 405 Talence, France

ARTICLE INFO

Article history:
Received 17 September 2008
Received in revised form 4 December 2008
Accepted 6 December 2008
Available online 24 December 2008

MSC:
76N15
65M06

PACS:
47.11.Df
47.10.Ab
47.40.Nm

Keywords:
Lagrangian hydrodynamics
Cell-centered scheme
Generalized Riemann problem
Compressible flow
High-order finite volume methods
Unstructured mesh

ABSTRACT

We present a high-order cell-centered Lagrangian scheme for solving the two-dimensional gas dynamics equations on unstructured meshes. A node-based discretization of the numerical fluxes for the physical conservation laws allows to derive a scheme that is compatible with the geometric conservation law (GCL). Fluxes are computed using a nodal solver which can be viewed as a two-dimensional extension of an approximate Riemann solver. The first-order scheme is conservative for momentum and total energy, and satisfies a local entropy inequality in its semi-discrete form. The two-dimensional high-order extension is constructed employing the generalized Riemann problem (GRP) in the acoustic approximation. Many numerical tests are presented in order to assess this new scheme. The results obtained for various representative configurations of one and two-dimensional compressible fluid flows show the robustness and the accuracy of our new scheme.

1. Introduction

We are interested in solving the two-dimensional compressible gas dynamics equations written in the Lagrangian form. In this paper, we aim to present an original high-order cell-centered scheme devoted to this task. This scheme consists of the non-trivial high-order extension of the first-order Lagrangian scheme presented in [29]. The two-dimensional high-order extension is constructed using the generalized Riemann problem (GRP) methodology, which was introduced by Ben-Artzi and Falcovitz in [5,7] following the pioneering work of van Leer [41].

In Lagrangian hydrodynamics methods, a computational cell moves with the flow velocity. In practice, this means that the cell vertices move with a computed velocity, the cell faces being uniquely specified by the vertex positions. This ensures that there is no mass flux crossing the boundary of the Lagrangian moving cell. Thus, Lagrangian methods can capture contact discontinuity sharply in multimaterial fluid flows. However, in the Lagrangian framework, one has to discretize not only

E-mail address: maire@celia.u-bordeaux1.fr
URL: http://www.celia.u-bordeaux1.fr/~maire

0021-9991/$ - see front matter © 2008 Elsevier Inc. All rights reserved.
doi:10.1016/j.jcp.2008.12.007

the gas dynamics equations but also the vertex motion in order to move the mesh. Moreover, the numerical fluxes of the physical conservation laws must be determined in a compatible way with the vertex velocity so that the geometric conservation law (GCL) is satisfied, namely the rate of change of a Lagrangian volume has to be computed coherently with the node motion. This critical requirement is the cornerstone of any Lagrangian multi-dimensional scheme.

The most natural way to solve this problem employs a staggered discretization in which position, velocity and kinetic energy are centered at points, while density, pressure and internal energy are within cells. The dissipation of kinetic energy into internal energy through shock waves is ensured by an artificial viscosity term. Since the seminal works of von Neumann and Richtmyer [43], and Wilkins [44], many developments have been made in order to improve the accuracy and the robustness of staggered hydrodynamics [12,10,8]. More specifically, the construction of a compatible staggered discretization leads to a scheme that conserves total energy in a rigorous manner [11,9].

We note also the recent development of a variational multi-scale stabilized approach in finite element computation of Lagrangian hydrodynamics, where a piecewise linear approximation was adopted for the variables [36,35]. The case of Q1/P0 finite element is studied in [37], where the kinematic variables are represented using a piecewise linear continuous approximation, while the thermodynamic variables utilize a piecewise constant representation.

An alternative to the previous discretizations is to derive a Lagrangian scheme based on the Godunov method [21]. In comparison to staggered discretizations, Godunov-type methods exhibit the good property of being naturally conservative, they do not need an artificial viscosity and they allow a straightforward implementation of conservative remapping methods when they are used in the context of the Arbitrary Lagrangian Eulerian (ALE) strategy. In the Godunov-type method approach, all conserved quantities, including momentum, and hence cell velocity are cell-centered. The cell-face quantities, including a face-normal component of the velocity, are available from the solution of an approximate Riemann problem at each cell face. However, it remains to determine the vertex velocity in order to move the mesh. In [1], Dukowicz has proposed to use a weighted least squares algorithm to compute the vertex velocity by requiring that the vertex velocity projected in the direction of a face normal should equal the Riemann velocity on that face. It turns out that this algorithm is capable of generating additional spurious components in the vertex velocity field. Hence, it leads to an artificial grid motion which requires a very expensive treatment [19]. This flaw comes probably from the fact that the flux computation is not compatible with the node displacement, and hence the GCL is not satisfied. An important achievement concerning the compatibility between flux discretization and vertex velocity computation has been introduced by Després and Mazeran [17]. In this paper, they present a scheme in which the interface fluxes and the node velocity are computed coherently thanks to an approximate Riemann solver located at the nodes. This original approach leads to a first-order conservative scheme which satisfies a local semi-discrete entropy inequality. The multi-dimensional high-order extension of this scheme is developed in [13]. A thorough study of the properties of the Després–Mazeran nodal solver shows a strong sensitivity to the cell aspect ratio, refer to [29], which can lead to severe numerical instabilities. This drawback is critical for real-life Lagrangian computations in which the grid often contains high aspect ratio cells. To overcome this difficulty, Maire et al. [29] have proposed an alternative scheme that successfully solves the aspect ratio problem and keeps the compatibility between fluxes discretization and vertices velocity computation. This first-order scheme also conserves momentum, total energy, and fulfills a local entropy inequality. Its main feature lies in the discretization of the pressure gradient, which is designed using two pressures at each node of a cell, each nodal pressure being associated with the direction of the unit outward normals related to the edges originating from the node. These nodal pressures are linked to the nodal velocity thanks to half-Riemann problems.

In the present paper, we describe the high-order extension of the previous cell-centered scheme. This high-order extension is derived using a one-step time integrator, based on the GRP method, which is cheaper than the classical two-steps Runge–Kutta procedure. The present approach consists in solving the high-order Riemann problem with piecewise linear polynomials, whereby the approximate solution is given as a time power series expansion right at the interface, thus providing a numerical flux for high-order Godunov methods. We have implemented the acoustic version of the GRP method, and extended it to the framework of our two-dimensional approximate Riemann solver located at the node. Hence, we get an acoustic generalized Riemann solver located at nodes, which enables us to compute the time derivatives of the nodal velocity and pressures, needed for the high-order flux computation. This solver is simple, robust and can handle tabulated equations of state provided that the isentropic sound speed is available. In addition, for one-dimensional flows aligned with the grid, it recovers the one-dimensional acoustic GRP scheme derived by Ben-Artzi and Falcovitz in their monograph [7].

The remainder of this paper is structured as follows: the governing equations of Lagrangian hydrodynamics are described in Section 2. For sake of completeness, the first-order discretization is revisited in Section 3. We also introduce the concept of sub-cell forces, borrowed from the staggered discretization framework [11], in order to derive a general form of the cell-centered discretization. The acoustic GRP high-order extension of the scheme is detailed in Section 4. Criteria for time step limitation are presented in Section 5. Extensive numerical experiments are reported in Section 6. They show not only the robustness and the accuracy of the present method but also its ability to handle successfully complex two-dimensional flows. More specifically, we show that our method satisfies the requirement of wavefront invariance and is able to compute properly isentropic compression [10]. Concluding remarks and perspectives are given in Section 7.

2. Lagrangian hydrodynamics

Let $\mathcal{D}$ be an open subset of $\mathbb{R}^2$, filled with an inviscid ideal fluid and equipped with the orthonormal frame $(0,X,Y)$ and the orthonormal basis $(\boldsymbol{e}_X, \boldsymbol{e}_Y)$. We also define the unit vector $\boldsymbol{e}_Z = \boldsymbol{e}_X \times \boldsymbol{e}_Y$. We are interested in discretizing the equations of the

Lagrangian hydrodynamics. It is convenient, from the point of view of subsequent discretization to write the unsteady compressible gas dynamics equations in the control volume formulation which holds for an arbitrary moving control volume. In the Lagrangian formalism the rates of change of mass, volume, momentum and total energy are computed assuming that the computational volumes are following the material motion. This leads to the following set of equations:

$$\frac{d}{dt}\int_{V(t)} \rho\, dV = 0, \tag{1a}$$

$$\frac{d}{dt}\int_{V(t)} dV - \int_{S(t)} \boldsymbol{U}\cdot\boldsymbol{N}\, dS = 0, \tag{1b}$$

$$\frac{d}{dt}\int_{V(t)} \rho\boldsymbol{U} dV + \int_{S(t)} P\boldsymbol{N}\, dS = 0, \tag{1c}$$

$$\frac{d}{dt}\int_{V(t)} \rho E dV + \int_{S(t)} P\boldsymbol{U}\cdot\boldsymbol{N}\, dV = 0, \tag{1d}$$

where $\frac{d}{dt}$ denotes the material, or Lagrangian, time derivative. Here, $V(t)$ is the moving control volume, and $S(t)$ its boundary. ρ, $\boldsymbol{U} = (u, v)^t$, P, E are the mass density, velocity, pressure and specific total energy of the fluid. $\boldsymbol{N}$ denotes the unit outward normal vector to the moving boundary $S(t)$. Eqs. (1a)–(1c) express the conservation of mass, momentum and total energy. We note that volume variation Eq. (1b) is also named geometric conservation law (GCL) and, it is equivalent to the local kinematic equation

$$\frac{d\boldsymbol{X}}{dt} = \boldsymbol{U}, \quad \boldsymbol{X}(0) = \boldsymbol{x}, \tag{2}$$

where $\boldsymbol{X}$ stands for coordinates defining the control volume surface at time $t > 0$ and $\boldsymbol{x}$ stands for coordinates at time $t = 0$. Then, $\boldsymbol{X} = \boldsymbol{X}(\boldsymbol{x}, t)$ is implicitly defined by the local kinematic equation, which is also called the trajectory equation. This enables us to define the map

$$\begin{aligned} &\mathcal{M}_t : V(0) \to V(t) \\ &\boldsymbol{x} \mapsto \boldsymbol{X}(\boldsymbol{x}, t), \end{aligned}$$

where $\boldsymbol{X}$ is the unique solution of (2). With fixed t, this map advances each fluid particle from its position at time $t = 0$ to its position at time t. Let J be the determinant of the Jacobian matrix of this map. Then, time differentiation of J gives the classical equation [14]

$$\frac{dJ}{dt} - J\nabla\cdot\boldsymbol{U} = 0,$$

which is nothing but the local version of the GCL Eq. (1b).

The thermodynamical closure of the set of Eq. (1) is obtained by the addition of an equation of state which is taken to be of the form

$$P = P(\rho, \varepsilon), \tag{3}$$

where the specific internal energy, ε, is related to the specific total energy by $\varepsilon = E - \frac{1}{2}\|\boldsymbol{U}\|^2$. The set of previous equations is referred to as the Lagrangian integral form of the Euler equations and can be found in many papers [1].

Comment 1. We notice that Eq. (1a) implies that the mass of the control volume remains constant.

3. First-order spatial discretization

3.1. Notations and assumptions

Let us consider the physical domain $V(0)$ that is initially filled with the fluid. We assume that we can map it by a set of polygonal cells without gaps or overlaps. Each cell is assigned a unique index c, and is denoted by $\Omega_c(0)$. Using the $\mathcal{M}_t$ map previously defined, we set $\Omega_c(t) = \mathcal{M}_t[\Omega_c(0)]$. Here, we assume that $\Omega_c(t)$ is still a polygon, that is, the $\mathcal{M}_t$ map is a continuous and linear function over each element of the mesh. Each point (vertex) of the mesh is assigned a unique index p and we denote by $\mathcal{P}(c)$ the counterclockwise ordered list of points of cell c.

3.2. Face flux discretization for the polygonal cell $\Omega_c(t)$

To get the discrete evolution equations for the primary variables $\left(\frac{1}{\rho}, \boldsymbol{U}, E\right)$ we apply the control volume formulation (1) to the polygonal cell $\Omega_c(t)$. Let m_c denotes the mass of the cell: it is constant according to (1). For a flow variable ϕ, we introduce its mass averaged value over the cell $\Omega_c(t)$

$$\phi_c = \frac{1}{m_c} \int_{\Omega_c(t)} \rho \phi \, dV.$$

Then, system (1) is written

$$m_c \frac{d}{dt}\left(\frac{1}{\rho_c}\right) - \sum_{f \in \mathcal{F}(c)} L_f^c \boldsymbol{U}_f^c \cdot \boldsymbol{N}_f^c = 0, \tag{4a}$$

$$m_c \frac{d}{dt}\boldsymbol{U}_c + \sum_{f \in \mathcal{F}(c)} L_f^c \Pi_f^c \boldsymbol{N}_f^c = 0, \tag{4b}$$

$$m_c \frac{d}{dt} E_c + \sum_{f \in \mathcal{F}(c)} L_f^c (\Pi \boldsymbol{U})_f^c \cdot \boldsymbol{N}_f^c = 0. \tag{4c}$$

Here, we have used the index f to denote a generic face of the cell c, L_f^c is the length of this face and $\boldsymbol{N}_f^c$ its unit outward normal and $\mathcal{F}(c)$ is the set of faces of cell c, cf. Fig. 1. We have also introduced the face fluxes $\boldsymbol{U}_f^c$, Π_f^c, $(\Pi \boldsymbol{U})_f^c$ which are defined as

$$\boldsymbol{U}_f^c = \frac{1}{L_f^c} \int_f \boldsymbol{U} dS, \tag{5a}$$

$$\Pi_f^c = \frac{1}{L_f^c} \int_f P dS, \tag{5b}$$

$$(\Pi \boldsymbol{U})_f^c = \frac{1}{L_f^c} \int_f P \boldsymbol{U} dS. \tag{5c}$$

The local kinematic equation in its discrete form at point p is written

$$\frac{d}{dt}\boldsymbol{X}_p = \boldsymbol{U}_p, \quad \boldsymbol{X}_p(0) = \boldsymbol{x}_p, \tag{6}$$

where $\boldsymbol{X}_p = (X_p, Y_p)^t$ denotes the coordinates of point p at time $t > 0$, $\boldsymbol{x}_p$ its initial position and $\boldsymbol{U}_p$ its velocity.

System (4) represents the face flux discretization of the Lagrangian hydrodynamics equations for the discrete variables $\left(\frac{1}{\rho_c}, \boldsymbol{U}_c, E_c\right)$. In order to compute the time evolution of the flow variables, we need to calculate the face fluxes $\boldsymbol{U}_f^c$, Π_f^c and $(\Pi \boldsymbol{U})_f^c$. Moreover, we also need to compute the point velocity $\boldsymbol{U}_p$ to move the mesh.

Comment 2. Eq. (4a) is not only a physical conservation law but also a geometrical one since $\frac{m_c}{\rho_c} = V_c$, where V_c is the volume of the cell c. The face flux $\boldsymbol{U}_f^c$ related to this equation must be computed consistently with the point velocity $\boldsymbol{U}_p$ so that the volume variation remains coherent with the mesh motion. This critical question is addressed in the next section.

3.3. Compatible discretization of the GCL

Since $m_c/\rho_c = V_c$ Eq. (4a) can be rewritten

$$\frac{dV_c}{dt} - \sum_{f \in \mathcal{F}(c)} L_f^c \boldsymbol{U}_f^c \cdot \boldsymbol{N}_f^c = 0.$$

The volume of cell c, V_c, is a function of the coordinates $\boldsymbol{X}_p$ of point p for $p \in \mathcal{P}(c)$. We compute this volume by performing the triangular decomposition of the cell displayed in Fig. 2

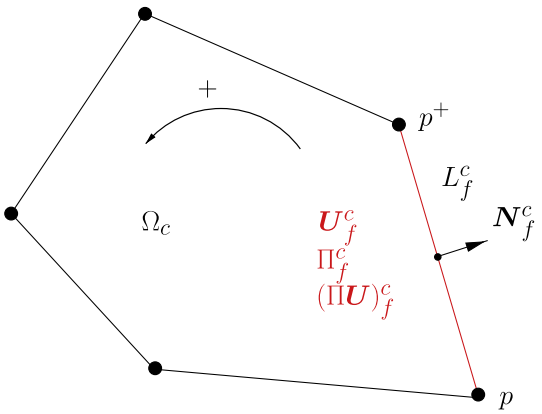

Fig. 1. Notations related to the polygonal cell $\Omega_c(t)$.

$$V_c = \frac{1}{2}\sum_{p\in\mathcal{P}(c)} (\boldsymbol{X}_p \times \boldsymbol{X}_{p^+}) \cdot \boldsymbol{e}_Z.$$

The time differentiation of this equation leads to

$$\frac{dV_c}{dt} = \sum_{p\in\mathcal{P}(c)} \frac{1}{2}(L_{pp^-}\boldsymbol{N}_{pp^-} + L_{pp^+}\boldsymbol{N}_{pp^+}) \cdot \boldsymbol{U}_p, \tag{7}$$

where the lengths L_{pp^-}, L_{pp^+} and the unit outward normal $\boldsymbol{N}_{pp^-}$, $\boldsymbol{N}_{pp^+}$ are related to the edges $[p, p^-]$ and $[p, p^+]$, see Fig. 2. By shifting indices in the previous summation, Eq. (7) becomes

$$\frac{dV_c}{dt} = \sum_{p\in\mathcal{P}(c)} L_{pp^+}\boldsymbol{N}_{pp^+} \cdot \frac{1}{2}(\boldsymbol{U}_p + \boldsymbol{U}_{p^+}). \tag{8}$$

Now, the comparison between Eqs. (4a) and (8) shows that they are equivalent under the condition that the face velocity is written

$$\boldsymbol{U}_f^c = \frac{1}{2}(\boldsymbol{U}_p + \boldsymbol{U}_{p^+}), \tag{9}$$

where the face f corresponds to the edge $[p, p^+]$. We remark that this condition amounts to a linear interpolation of the velocity along the edge $[p, p^+]$. The only way to satisfy the compatibility condition (9) consists in first computing the point velocity $\boldsymbol{U}_p$ then, deducing the face velocity $\boldsymbol{U}_f^c$. By proceeding in this manner, the compatibility of the face discretization of the GCL with the rate of change of the cell volume is ensured. Let us introduce the following notations (see Fig. 2)

$$L_{\underline{p}}^c = \frac{1}{2}L_{pp^-}, \quad \boldsymbol{N}_{\underline{p}}^c = \boldsymbol{N}_{pp^-},$$
$$L_{\overline{p}}^c = \frac{1}{2}L_{pp^+}, \quad \boldsymbol{N}_{\overline{p}}^c = \boldsymbol{N}_{pp^+},$$

then, Eq. (7) writes:

$$\frac{dV_c}{dt} = \sum_{p\in\mathcal{P}(c)} (L_{\underline{p}}^c\boldsymbol{N}_{\underline{p}}^c + L_{\overline{p}}^c\boldsymbol{N}_{\overline{p}}^c) \cdot \boldsymbol{U}_p. \tag{10}$$

Comment 3. Following Shashkov [38], we introduce $(\nabla \cdot \boldsymbol{U})_c$ the discrete divergence operator over cell c

$$(\nabla \cdot \boldsymbol{U})_c = \frac{1}{V_c}\int_{\partial\Omega_c} \boldsymbol{U} \cdot \boldsymbol{N} dS.$$

Combining the previous results and this definition we get

$$(\nabla \cdot \boldsymbol{U})_c = \frac{1}{V_c}\frac{dV_c}{dt} = \frac{1}{V_c}\sum_{p\in\mathcal{P}(c)} (L_{\underline{p}}^c\boldsymbol{N}_{\underline{p}}^c + L_{\overline{p}}^c\boldsymbol{N}_{\overline{p}}^c) \cdot \boldsymbol{U}_p = \frac{1}{V_c}\sum_{p\in\mathcal{P}(c)} L_{pc}\boldsymbol{N}_{pc} \cdot \boldsymbol{U}_p,$$

where $\boldsymbol{N}_{pc}$ stands for the unit corner vector defined by $L_{pc}\boldsymbol{N}_{pc} = L_{\underline{p}}^c\boldsymbol{N}_{\underline{p}}^c + L_{\overline{p}}^c\boldsymbol{N}_{\overline{p}}^c$. We have recovered the compatible discretization of the divergence operator currently used in the derivation of the compatible Lagrangian hydrodynamics scheme [11].

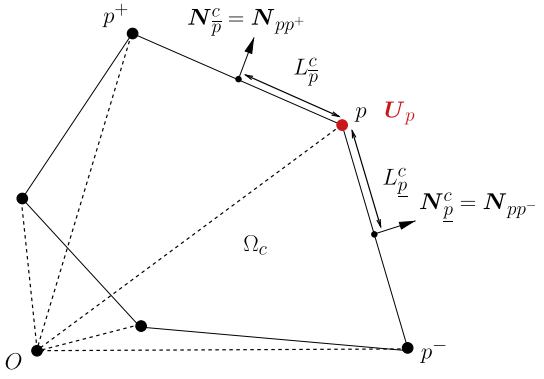

Fig. 2. Triangular decomposition of the polygonal cell $\Omega_c(t)$.

3.4. Computation of the momentum flux

To ensure consistency with the GCL discretization we propose to discretize the momentum flux by introducing two pressures at each node p of cell c. These pressures are denoted $\Pi_{\underline{p}}^c$ and $\Pi_{\bar{p}}^c$, see Fig. 3, they can be seen as nodal pressures viewed from cell c and related to the two edges impinging at node p. Using these nodal pressures, we propose the following definition of the discrete gradient operator over the cell c

$$(\nabla P)_c = \frac{1}{V_c} \sum_{p \in \mathcal{P}(c)} \left(L_{\underline{p}}^c \Pi_{\underline{p}}^c \boldsymbol{N}_{\underline{p}}^c + L_{\bar{p}}^c \Pi_{\bar{p}}^c \boldsymbol{N}_{\bar{p}}^c \right).$$

This definition is compatible with the previous result related to the discrete divergence operator. Using the discrete gradient operator, the momentum equation is rewritten

$$m_c \frac{d}{dt} \boldsymbol{U}_c + \sum_{p \in \mathcal{P}(c)} \left(L_{\underline{p}}^c \Pi_{\underline{p}}^c \boldsymbol{N}_{\underline{p}}^c + L_{\bar{p}}^c \Pi_{\bar{p}}^c \boldsymbol{N}_{\bar{p}}^c \right) = 0. \tag{11}$$

We have obtained a nodal flux discretization for the momentum equation which is equivalent to its face flux discretization (4b) provided that the momentum face flux is written

$$\Pi_f^c = \frac{1}{2} (\Pi_{\bar{p}}^c + \Pi_{\underline{p}^+}^c).$$

Once again, we note that this condition amounts to a linear interpolation of the pressure along face $f = [p, p^+]$.

The examination of the right-hand side of Eq. (11) allows a mechanical interpretation by introducing the force

$$\boldsymbol{F}_{pc} = L_{\underline{p}}^c \Pi_{\underline{p}}^c \boldsymbol{N}_{\underline{p}}^c + L_{\bar{p}}^c \Pi_{\bar{p}}^c \boldsymbol{N}_{\bar{p}}^c. \tag{12}$$

This force is a sub-cell force related to point p and cell c. Using this definition, the momentum equation can also be written

$$m_c \frac{d}{dt} \boldsymbol{U}_c + \sum_{p \in \mathcal{P}(c)} \boldsymbol{F}_{pc} = 0. \tag{13}$$

To close this section, we show how to express the nodal pressures. Since the velocity of the edges $[p, p^-]$ and $[p, p^+]$, in the vicinity of point p, is equal to the nodal velocity $\boldsymbol{U}_p$, the nodal pressures are computed using the following half approximate Riemann problems

$$P_c - \Pi_{\underline{p}}^c = Z_{\underline{p}}^c (\boldsymbol{U}_p - \boldsymbol{U}_c) \cdot \boldsymbol{N}_{\underline{p}}^c, \tag{14a}$$

$$P_c - \Pi_{\bar{p}}^c = Z_{\bar{p}}^c (\boldsymbol{U}_p - \boldsymbol{U}_c) \cdot \boldsymbol{N}_{\bar{p}}^c. \tag{14b}$$

Here, $Z_{\underline{p}}^c$, $Z_{\bar{p}}^c$ are mass fluxes swept by the waves. To determine these coefficients we follow the approach suggested by Dukowicz [18] by setting

$$Z_{\underline{p}}^c = \rho_c [a_c + \Gamma_c |(\boldsymbol{U}_p - \boldsymbol{U}_c) \cdot \boldsymbol{N}_{\underline{p}}^c|], \tag{15a}$$

$$Z_{\bar{p}}^c = \rho_c [a_c + \Gamma_c |(\boldsymbol{U}_p - \boldsymbol{U}_c) \cdot \boldsymbol{N}_{\bar{p}}^c|], \tag{15b}$$

where a_c is the local isentropic speed of sound and Γ_c is a material-dependent parameter that is given in terms of the density ratio in the limit of very strong shocks. In the case of gamma law gas one gets $\Gamma_c = \frac{\gamma+1}{2}$. We note that for $\Gamma_c = 0$, we recover the classical acoustic approximation and the coefficients $Z_{\underline{p}}^c$ and $Z_{\bar{p}}^c$ reduce to the acoustic impedance of cell c.

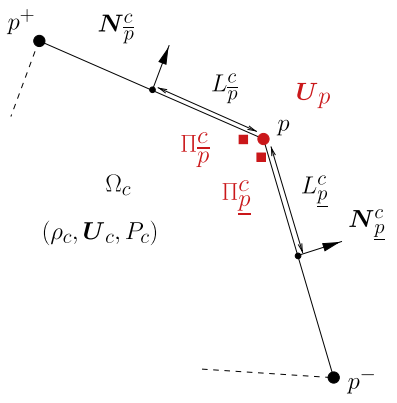

Fig. 3. Localization of the nodal pressures given by the half Riemann problems at point p viewed from cell Ω_c.

Utilizing (14), the sub-cell force can be rewritten

$$\boldsymbol{F}_{pc} = L_{pc} P_c \boldsymbol{N}_{pc} - \mathsf{M}_{pc}(\boldsymbol{U}_p - \boldsymbol{U}_c), \tag{16}$$

where $L_{pc}\boldsymbol{N}_{pc} = L^c_{\underline{p}}\boldsymbol{N}^c_{\underline{p}} + L^c_{\bar{p}}\boldsymbol{N}^c_{\bar{p}}$ is the corner vector related to point p and cell c, and $\mathsf{M}_{pc} = Z^c_{\underline{p}} L^c_{\underline{p}} (\boldsymbol{N}^{\boldsymbol{c}}_{\underline{\boldsymbol{p}}} \otimes \boldsymbol{N}^{\boldsymbol{c}}_{\underline{\boldsymbol{p}}}) + Z^c_{\bar{p}} L^c_{\bar{p}} (\boldsymbol{N}^{\boldsymbol{c}}_{\bar{\boldsymbol{p}}} \otimes \boldsymbol{N}^{\boldsymbol{c}}_{\bar{\boldsymbol{p}}})$ is a 2×2 symmetric positive definite matrix. The second term in the right-hand side of Eq. (16) can be viewed as the tensorial part of the sub-cell force.

Comment 4. We have introduced two pressures at node p, each pressure being associated with the unit outward normal related to the two edges of cell c impinging at point p. Instead of that, one can introduce only one pressure at point p. This pressure is determined by the half Riemann problem defined in the direction of the unit corner vector $\boldsymbol{N}_{pc}$

$$P_c - \Pi_{pc} = Z_c(\boldsymbol{U}_p - \boldsymbol{U}_c) \cdot \boldsymbol{N}_{pc}, \tag{17}$$

where Z_c is the acoustic impedance of cell c.

This amounts to define only one nodal pressure Π_{pc} for each cell that surrounds point p. Using the unit corner vector $\boldsymbol{N}_{pc}$ in the definition of the half Riemann problem, we have recovered the approach developed in [17]. The sub-cell force corresponding to this single nodal pressure Π_{pc} reads

$$\boldsymbol{F}_{pc} = L_{pc}\Pi_{pc}\boldsymbol{N}_{pc} = L_{pc}P_c\boldsymbol{N}_{pc} - \mathbb{M}_{pc}(\boldsymbol{U}_p - \boldsymbol{U}_c),$$

where $\mathbb{M}_{pc} = L_{pc} Z_c \boldsymbol{N}_{pc} \otimes \boldsymbol{N}_{pc}$ is a 2×2 symmetric positive matrix. We note that this sub-cell force is always colinear to the geometric direction $\boldsymbol{N}_{pc}$ of the unit corner vector. Moreover, its tensorial part is different from the one of sub-cell force $\boldsymbol{F}_{pc}$. For numerical applications, it appears that the approach proposed in [17] exhibits a strong dependence to the cell aspect ratio as it has been noticed in [29].

3.5. Computation of the total energy flux

The total energy flux computation is performed by using the previous mechanical interpretation based on the sub-cell force $\boldsymbol{F}_{pc}$. Thus, the time rate of change of total energy is equal to the summation of the works performed by the sub-cell forces over the cell c

$$m_c \frac{d}{dt} E_c + \sum_{p \in \mathcal{P}(c)} \boldsymbol{F}_{pc} \cdot \boldsymbol{U}_p = 0. \tag{18}$$

The substitution of the sub-cell force definition (12) in the previous equation leads to the following node flux discretization of the total energy equation

$$m_c \frac{d}{dt} E_c + \sum_{p \in \mathcal{P}(c)} (L^c_{\underline{p}} \Pi^c_{\underline{p}} \boldsymbol{N}^{\boldsymbol{c}}_{\underline{\boldsymbol{p}}} + L^c_{\bar{p}} \Pi^c_{\bar{p}} \boldsymbol{N}^{\boldsymbol{c}}_{\bar{\boldsymbol{p}}}) \cdot \boldsymbol{U}_p = 0. \tag{19}$$

We claim that this node flux discretization is equivalent to the face flux discretization (4c) provided that the total energy flux is written

$$(\Pi \boldsymbol{U})^c_f = \frac{1}{2}(\Pi^c_{\bar{p}} \boldsymbol{U}_p + \Pi^c_{\underline{p}^+} \boldsymbol{U}_{p^+}).$$

3.6. Node flux discretization for the polygonal cell $\Omega_c(t)$

Gathering the results from previous sections, we write the semi-discrete evolution equations for the unknowns $\left(\frac{1}{\rho_c}, \boldsymbol{U}_c, E_c\right)$

$$m_c \frac{d}{dt}\left(\frac{1}{\rho_c}\right) - \sum_{p \in \mathcal{P}(c)} (L^c_{\underline{p}} \boldsymbol{N}^c_{\underline{p}} + L^c_{\bar{p}} \boldsymbol{N}^c_{\bar{p}}) \cdot \boldsymbol{U}_p = 0, \tag{20a}$$

$$m_c \frac{d}{dt} \boldsymbol{U}_c + \sum_{p \in \mathcal{P}(c)} (L^c_{\underline{p}} \Pi^c_{\underline{p}} \boldsymbol{N}^c_{\underline{p}} + L^c_{\bar{p}} \Pi^c_{\bar{p}} \boldsymbol{N}^c_{\bar{p}}) = 0, \tag{20b}$$

$$m_c \frac{d}{dt} E_c + \sum_{p \in \mathcal{P}(c)} (L^c_{\underline{p}} \Pi^c_{\underline{p}} \boldsymbol{N}^c_{\underline{p}} + L^c_{\bar{p}} \Pi^c_{\bar{p}} \boldsymbol{N}^c_{\bar{p}}) \cdot \boldsymbol{U}_p = 0. \tag{20c}$$

This system is based on a node flux discretization, it is equivalent to system (4) provided that the face fluxes are written

$$\boldsymbol{U}^c_f = \frac{1}{2}(\boldsymbol{U}_p + \boldsymbol{U}_{p^+}), \tag{21a}$$

$$\Pi^c_f = \frac{1}{2}(\Pi^c_{\bar{p}} + \Pi^c_{\underline{p}^+}), \tag{21b}$$

$$(\Pi \boldsymbol{U})^c_f = \frac{1}{2}(\Pi^c_{\bar{p}} \boldsymbol{U}_p + \Pi^c_{\underline{p}^+} \boldsymbol{U}_{p^+}), \tag{21c}$$

where face f represents the edge $[p, p^+]$, see Fig. 3. We recall that the nodal pressures are expressed as a function of the node velocity by using the half approximate Riemann problems (14). The displacement of the mesh is governed by the local kinematic equation written in discrete form at point p (6).

To close system (20) we need to determine the point velocity $\boldsymbol{U}_p$. This goal will be achieved next section constructing a nodal solver.

3.7. Construction of a nodal solver

The aim of this section is to construct a nodal solver in order to compute the nodal velocity and the nodal pressures. The evaluation of these nodal quantities relies on an argument of conservation concerning both momentum and total energy.

3.7.1. Momentum and total energy conservation

First, let us show why the interface pressure on each face is not uniquely defined, contrary to the classical finite volume approach. Consider the face $[p,q]$ shared by the cells Ω_c and Ω_d. As it is displayed in Fig. 4, we have two nodal pressures on $[p,q]$ viewed from cell c: $\Pi_{\underline{p}}^c, \Pi_{\underline{q}}^c$, and two nodal pressures on $[p,q]$ viewed from cell d : $\Pi_{\underline{p}}^d, \Pi_{\underline{q}}^d$. The nodal pressures related to node p are written according to Eq. (14)

$$P_c - \Pi_{\underline{p}}^c = Z_c(\boldsymbol{U}_p - \boldsymbol{U}_c)\cdot \boldsymbol{N}_{\underline{p}}^c,$$
$$P_d - \Pi_{\underline{p}}^d = -Z_d(\boldsymbol{U}_p - \boldsymbol{U}_d)\cdot \boldsymbol{N}_{\underline{p}}^c.$$

Note that here, in order to simplify the computations, we have used the acoustic approximate Riemann solver. Hence, Z_c, Z_d denote the acoustic impedance of cells c and d.

By subtracting the second equation from the first one we obtain

$$\Pi_{\underline{p}}^d - \Pi_{\underline{p}}^c = (Z_c + Z_d)(\boldsymbol{U}_p \cdot \boldsymbol{N}_{\underline{p}}^c - \mathcal{V}), \tag{22}$$

where $\mathcal{V}$ is nothing but the normal component of the Riemann velocity

$$\mathcal{V} = \frac{Z_c\boldsymbol{U}_c + Z_d\boldsymbol{U}_d}{Z_c + Z_d}\cdot \boldsymbol{N}_{\underline{p}}^c - \frac{P_d - P_c}{Z_c + Z_d}.$$

This velocity corresponds to the one-dimensional solution of the acoustic Riemann problem in the direction of the unit normal $\boldsymbol{N}_{\underline{p}}^c$. Eq. (22) shows that the nodal pressures are equal if and only if the projection of the node velocity onto the unit normal is equal to the one-dimensional normal component of the Riemann velocity. Since in general $\boldsymbol{U}_p \cdot \boldsymbol{N}_{\underline{p}}^c \neq \mathcal{V}$, we have the discontinuity $\Pi_{\underline{p}}^d \neq \Pi_{\underline{p}}^c$. The discontinuity of these nodal pressures across the face implies the loss of momentum and total energy conservation, on the contrary to the 1-D Riemann solver classical approach. We shall show hereafter how to recover momentum and total energy conservation by imposing an additional constraint which will be the main ingredient to construct the nodal solver.

To examine momentum conservation, let us write the global balance of momentum without taking into account the boundary conditions. The summation of the momentum Eq. (13) over all the cells c leads to

$$\frac{d}{dt}\sum_c m_c\boldsymbol{U}_c = -\sum_c \sum_{p\in\mathcal{P}(c)} \boldsymbol{F}_{pc}. \tag{23}$$

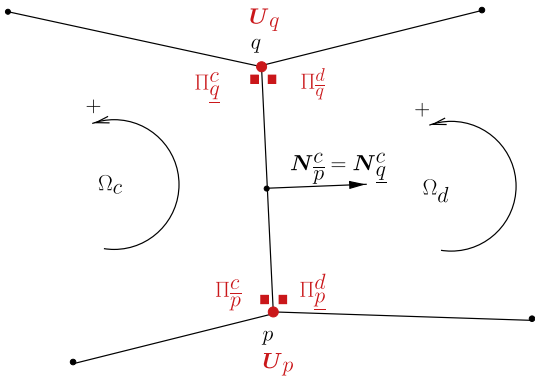

Fig. 4. Nodal pressures related to the face $[p,q]$ shared by cells Ω_c and Ω_d.

Switching the summation over cells and the summation over nodes in right-hand side of (23) one gets

$$\frac{d}{dt}\sum_c m_c \boldsymbol{U}_c = -\sum_p \sum_{c\in\mathcal{C}(p)} \boldsymbol{F}_{pc},$$

where $\mathcal{C}(p)$ is the set of the cells around point p. Then, momentum conservation is ensured provided that the sub-cell forces satisfy the condition

$$\sum_{c\in\mathcal{C}(p)} \boldsymbol{F}_{pc} = 0. \tag{24}$$

We claim that, if this condition is satisfied then total energy is also conserved. To demonstrate this property we perform the summation of the total energy Eq. (18) over all the cells c

$$\frac{d}{dt}\sum_c m_c E_c = -\sum_c \sum_{p\in\mathcal{P}(c)} \boldsymbol{F}_{pc}\cdot\boldsymbol{U}_p.$$

Then, we switch again the summation over cells and the summation over nodes in right-hand side to get

$$\frac{d}{dt}\sum_c m_c E_c = -\sum_p \sum_{c\in\mathcal{C}(p)} \boldsymbol{F}_{pc}\cdot\boldsymbol{U}_p.$$

Due to (24) the term between parentheses in the right-hand side is null and the total energy is conserved.

We note that the sufficient condition (24) expresses the balance of the sub-cell forces around point p (refer to Fig. 5). Using the definition of the sub-cell force it can be rewritten

$$\sum_{c\in\mathcal{C}(p)} (L_{\underline{p}}^c \Pi_{\underline{p}}^c \boldsymbol{N}_{\underline{p}}^c + L_{\bar{p}}^c \Pi_{\bar{p}}^c \boldsymbol{N}_{\bar{p}}^c) = 0. \tag{25}$$

Now, using the equation of the sub-cell force (16) in which nodal pressures are expressed thanks to the half Riemann problems, we obtain the final form

$$\sum_{c\in\mathcal{C}(p)} [L_{pc} P_c \boldsymbol{N}_{pc} - \mathsf{M}_{pc}(\boldsymbol{U}_p - \boldsymbol{U}_c)] = 0. \tag{26}$$

We recall that $L_{pc}\boldsymbol{N}_{pc} = L_{\underline{p}}^c \boldsymbol{N}_{\underline{p}}^c + L_{\bar{p}}^c \boldsymbol{N}_{\bar{p}}^c$ is the corner vector related to point p, cell c and $\mathsf{M}_{pc} = Z_{\underline{p}}^c L_{\underline{p}}^c (\boldsymbol{N}_{\underline{p}}^c \otimes \boldsymbol{N}_{\underline{p}}^c) + Z_{\bar{p}}^c L_{\bar{p}}^c (\boldsymbol{N}_{\bar{p}}^c \otimes \boldsymbol{N}_{\bar{p}}^c)$ is a 2×2 symmetric positive definite matrix.

The sufficient condition to ensure momentum and total energy conservation exhibits, in its final form, a vectorial equation satisfied by the point velocity $\boldsymbol{U}_p$. This equation allows to construct a nodal solver.

3.7.2. The nodal solver

Setting $\mathsf{M}_p = \sum_{c\in\mathcal{C}(p)} \mathsf{M}_{pc}$ the system satisfied by the point velocity $\boldsymbol{U}_p$ is written

$$\mathsf{M}_p \boldsymbol{U}_p = \sum_{c\in\mathcal{C}(p)} (L_{pc} P_c \boldsymbol{N}_{pc} + \mathsf{M}_{pc}\boldsymbol{U}_c). \tag{27}$$

We remark that the M_p matrix is symmetric positive definite by construction, hence it is always invertible. If we use the acoustic approximation (coefficient $\Gamma_c = 0$ in Eq. (15)), the mass swept fluxes reduce to the acoustic impedance, i.e. $Z_{\underline{p}}^c = Z_{\bar{p}}^c = Z_c$, then the system (27) becomes linear and it admits a unique solution. It has been showed in [29] that this

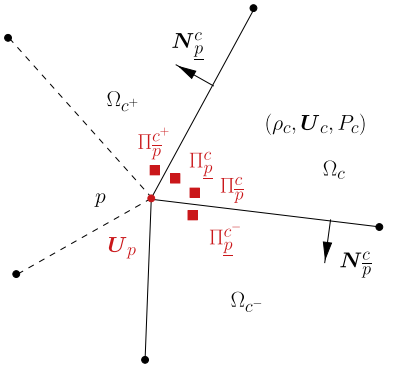

Fig. 5. Notations related to the nodal solver at point p.

two-dimensional acoustic solver reduces to the classical one-dimensional Godunov acoustic solver for one-dimensional flows either for Cartesian or cylindrical grid aligned with the flow. In the general case corresponding to $\Gamma_c \neq 0$, system (27) is non-linear due to the dependence of the mass swept fluxes to the point velocity. Therefore, $\boldsymbol{U}_p$ has to be computed by using an iterative procedure such as a fixed point algorithm. From a theoretical point of view, we cannot show convergence of such an algorithm. However, in numerical applications, we have found that few iterations are needed to get the convergence. Regardless of the type of approximation used, the expressions for the point velocity and the pressure fluxes can be written

$$\boldsymbol{U}_p = \mathsf{M}_p^{-1} \bar{\sum_{c\in\mathcal{C}(p)}} (L_{pc} P_c \boldsymbol{N}_{pc} + \mathsf{M}_{pc} \boldsymbol{U}_c), \tag{28a}$$

$$P_c - \Pi_{\underline{p}}^c = Z_{\underline{p}}^c (\boldsymbol{U}_p - \boldsymbol{U}_c) \cdot \boldsymbol{N}_{\underline{p}}^c, \tag{28b}$$

$$P_c - \Pi_{\bar{p}}^c = Z_{\bar{p}}^c (\boldsymbol{U}_p - \boldsymbol{U}_c) \cdot \boldsymbol{N}_{\bar{p}}^c. \tag{28c}$$

Comment 5. It is interesting to realize that this nodal solver only needs the knowledge of the isentropic speed of sound: it is very easy to extend it to more general equation of state. The precise form of the equation of state, analytical or tabulated, does not matter provided that the speed of sound is known.

3.8. Summary

In this section, we give a summary of the semi-discrete evolution equations that constitute a closed set for the unknowns $\left(\frac{1}{\rho_c}, \boldsymbol{U}_c, E_c\right)$

$$m_c \frac{d}{dt}\left(\frac{1}{\rho_c}\right) - \bar{\sum_{p\in\mathcal{P}(c)}} (L_{\underline{p}}^c \boldsymbol{N}_{\underline{p}}^c + L_{\bar{p}}^c \boldsymbol{N}_{\bar{p}}^c) \cdot \boldsymbol{U}_p = 0,$$

$$m_c \frac{d}{dt}\boldsymbol{U}_c + \bar{\sum_{p\in\mathcal{P}(c)}} (L_{\underline{p}}^c \Pi_{\underline{p}}^c \boldsymbol{N}_{\underline{p}}^c + L_{\bar{p}}^c \Pi_{\bar{p}}^c \boldsymbol{N}_{\bar{p}}^c) = 0,$$

$$m_c \frac{d}{dt} E_c + \bar{\sum_{p\in\mathcal{P}(c)}} (L_{\underline{p}}^c \Pi_{\underline{p}}^c \boldsymbol{N}_{\underline{p}}^c + L_{\bar{p}}^c \Pi_{\bar{p}}^c \boldsymbol{N}_{\bar{p}}^c) \cdot \boldsymbol{U}_p = 0.$$

The discrete kinematic equation

$$\frac{d}{dt}\boldsymbol{X}_p = \boldsymbol{U}_p, \quad \boldsymbol{X}_p(0) = \boldsymbol{x}_p$$

enables us to compute the mesh motion. The point velocity $\boldsymbol{U}_p$ and the nodal pressures are obtained thanks to the nodal solver

$$\boldsymbol{U}_p = \mathsf{M}_p^{-1} \bar{\sum_{c\in\mathcal{C}(p)}} (L_{pc} P_c \boldsymbol{N}_{pc} + \mathsf{M}_{pc} \boldsymbol{U}_c),$$

$$P_c - \Pi_{\underline{p}}^c = Z_{\underline{p}}^c (\boldsymbol{U}_p - \boldsymbol{U}_c) \cdot \boldsymbol{N}_{\underline{p}}^c,$$

$$P_c - \Pi_{\bar{p}}^c = Z_{\bar{p}}^c (\boldsymbol{U}_p - \boldsymbol{U}_c) \cdot \boldsymbol{N}_{\bar{p}}^c,$$

where the 2×2 matrices, M_{pc} and M_p, are written

$$\mathsf{M}_{pc} = Z_{\underline{p}}^c L_{\underline{p}}^c (\boldsymbol{N}_{\underline{\boldsymbol{p}}}^{\boldsymbol{c}} \otimes \boldsymbol{N}_{\underline{\boldsymbol{p}}}^{\boldsymbol{c}}) + Z_{\bar{p}}^c L_{\bar{p}}^c (\boldsymbol{N}_{\bar{\boldsymbol{p}}}^{\boldsymbol{c}} \otimes \boldsymbol{N}_{\bar{\boldsymbol{p}}}^{\boldsymbol{c}}), \quad \mathsf{M}_p = \bar{\sum_{c\in\mathcal{C}(p)}} \mathsf{M}_{pc}. \tag{29}$$

We recall that the swept mass fluxes $Z_{\underline{p}}^c$ and $Z_{\bar{p}}^c$ are defined by (15).

Finally, we have obtained a first-order cell-centered discretization of the Lagrangian hydrodynamics equations based on a node flux discretization. The fluxes and the mesh motion are computed in a compatible way thanks to a nodal solver that uniquely provides the point velocity and the nodal pressures.

Comment 6. In the Lagrangian formalism, we have to consider two types of boundary conditions on the border of the domain $\mathcal{D}$: either the pressure or the normal component of the velocity is prescribed. Here, we do not detail the implementation of these boundary conditions. Let us notice that they are consistent with our nodal solver. For a detailed presentation about this topic the reader can refer to [29].

3.9. Entropy inequality

We show that our first-order Lagrangian scheme in its semi-discrete form satisfies a local entropy inequality. Using the Gibbs formula [16], we compute the time rate of change of the specific entropy σ_c in cell c

$$m_c T_c \frac{d\sigma_c}{dt} = m_c \left[\frac{d\varepsilon_c}{dt} + P_c \frac{d}{dt}\left(\frac{1}{\rho_c}\right) \right], \tag{30}$$

where T_c denotes the mean temperature of the cell. Thanks to the definition of the internal energy this equation is rewritten

$$m_c T_c \frac{d\sigma_c}{dt} = m_c \left[\frac{dE_c}{dt} - \boldsymbol{U}_c \cdot \frac{d\boldsymbol{U}_c}{dt} + P_c \frac{d}{dt}\left(\frac{1}{\rho_c}\right) \right].$$

We dot-multiply momentum Eq. (13) by $\boldsymbol{U}_c$ and subtract it from the total energy Eq. (18) to get

$$m_c \left[\frac{dE_c}{dt} - \boldsymbol{U}_c \cdot \frac{d\boldsymbol{U}_c}{dt} \right] = - \bar{\sum_{p \in \mathcal{P}(c)}} \boldsymbol{F}_{pc} \cdot (\boldsymbol{U}_p - \boldsymbol{U}_c).$$

The pressure work is computed by multiplying (20a) by P_c

$$P_c \frac{d}{dt}\left(\frac{1}{\rho_c}\right) = \bar{\sum_{p \in \mathcal{P}(c)}} L_{pc} P_c \boldsymbol{N}_{pc} \cdot \boldsymbol{U}_p = \bar{\sum_{p \in \mathcal{P}(c)}} L_{pc} P_c \boldsymbol{N}_{pc} \cdot (\boldsymbol{U}_p - \boldsymbol{U}_c).$$

Here, we have introduced the corner vector $L_{pc}\boldsymbol{N}_{pc} = L_{\underline{p}}^{c}\boldsymbol{N}_{\underline{p}}^{c} + L_{p}^{c}\boldsymbol{N}_{p}^{c}$ related to point p. The last line of the previous equation comes from the fact that for a closed polygon we have

$$\bar{\sum_{p \in \mathcal{P}(c)}} L_{pc}\boldsymbol{N}_{pc} = 0.$$

Finally, the combination of the previous results leads to

$$m_c T_c \frac{d\sigma_c}{dt} = \bar{\sum_{p \in \mathcal{P}(c)}} (L_{pc} P_c \boldsymbol{N}_{pc} - \boldsymbol{F}_{pc}) \cdot (\boldsymbol{U}_p - \boldsymbol{U}_c). \tag{31}$$

With the help of the half Riemann problems (14), we have previously seen that the sub-cell force can be written $\boldsymbol{F}_{pc} = L_{pc} P_c \boldsymbol{N}_{pc} - \mathsf{M}_{pc}(\boldsymbol{U}_p - \boldsymbol{U}_c)$, using this, we deduce the final expression for the time rate of change of the specific entropy within cell c

$$m_c T_c \frac{d\sigma_c}{dt} = \bar{\sum_{p \in \mathcal{P}(c)}} \mathsf{M}_{pc}(\boldsymbol{U}_p - \boldsymbol{U}_c) \cdot (\boldsymbol{U}_p - \boldsymbol{U}_c). \tag{32}$$

Since the 2×2 matrix M_{pc} is symmetric positive definite, the right-hand side of (32) is a quadratic form which is always positive. Consequently, our scheme is such that entropy increases in the cell c, that is $\frac{d\sigma_c}{dt} \geqslant 0$. This important property ensures that the kinetic energy is properly dissipated in internal energy. The examination of (32) right-hand side shows a tensorial structure of the entropy dissipation rate which is quite similar to the artificial viscosity used in two-dimensional staggered Lagrangian schemes [8,10].

Comment 7. We note that Eq. (31) is quite general and has been obtained regardless the expression of the sub-cell force. Thus, it can be used to derive the entropy production corresponding to the scheme developed by Després and Mazeran [17]. In this case the sub-cell force is written $\boldsymbol{\mathcal{F}}_{pc} = L_{pc} P_c \boldsymbol{N}_{pc} - \mathcal{M}_{pc}(\boldsymbol{U}_p - \boldsymbol{U}_c)$ where $\mathcal{M}_{pc} = L_{pc} Z_c \boldsymbol{N}_{pc} \otimes \boldsymbol{N}_{pc}$ (refer to Comment 4). This choice provides the entropy production

$$m_c T_c \frac{d\sigma_c}{dt} = \bar{\sum_{p \in \mathcal{P}(c)}} \mathcal{M}_{pc}(\boldsymbol{U}_p - \boldsymbol{U}_c) \cdot (\boldsymbol{U}_p - \boldsymbol{U}_c).$$

The discrepancy corresponding to the entropy production between our scheme and the one proposed in [17] comes from the definition of the corner matrices M_{pc} and $\mathcal{M}_{pc}$. The entropy production of our scheme can only go to zero for uniform flows because the matrix M_{pc} is definite positive. In the case of the scheme developed by Després and Mazeran, the entropy production can go to zero even for non uniform flows such that $(\boldsymbol{U}_p - \boldsymbol{U}_c) \perp \boldsymbol{N}_{pc}$ since $\ker(\mathcal{M}_{pc})$ is spanned by $\boldsymbol{N}_{pc}^{\perp}$. This fact probably explains why the Després-Mazeran scheme can exhibit, for certain flows, severe numerical instabilities such as hourglass modes [13,33].

Comment 8. We must admit that our entropy production term is always active even in the case of isentropic flows. For such flows our scheme does not conserve entropy. This property is typical from Godunov-type schemes. However, this extra entropy production can be dramatically decreased by using a high-order extension of the scheme as we shall see in Section 4.

3.10. Discretization based on sub-cell forces

Throughout this paper we have used the sub-cell forces formalism. This general formalism is very useful and has been first introduced in [9,11] in the framework of staggered Lagrangian scheme. It turns out that this formalism can also be fruit-

fully utilized in the cell-centered Lagrangian scheme framework. In this context, we show that the sub-cell force formalism is the cornerstone to design a numerical scheme by using elementary physical arguments such as momentum, total energy conservation and entropy inequality.

First of all, we recall the Lagrangian hydrodynamics equations written using the sub-cell formalism

$$m_c \frac{d}{dt}\left(\frac{1}{\rho_c}\right) - \sum_{p\in\mathcal{P}(c)} L_{pc}\boldsymbol{N}_{pc}\cdot\boldsymbol{U}_p = 0, \tag{33a}$$

$$m_c \frac{d}{dt}\boldsymbol{U}_c + \sum_{p\in\mathcal{P}(c)} \boldsymbol{F}_{pc} = 0, \tag{33b}$$

$$m_c \frac{d}{dt}E_c + \sum_{p\in\mathcal{P}(c)} \boldsymbol{F}_{pc}\cdot\boldsymbol{U}_p = 0, \tag{33c}$$

where, as defined previously, the sub-cell force $\boldsymbol{F}_{pc}$ is

$$\boldsymbol{F}_{pc} = L_{\underline{p}}^c \Pi_{\underline{p}}^c \boldsymbol{N}_{\underline{p}}^c + L_{\overline{p}}^c \Pi_{\overline{p}}^c \boldsymbol{N}_{\overline{p}}^c.$$

The time rate change of entropy associated with this scheme can be derived exactly in the same manner as in the previous section. Then, we obtain the general Eq. (31) whatever the sub-cell force is. If we carefully observe the right-hand side of (31), it appears clearly that the sub-cell force can be split into an isentropic and a viscous part as follows:

$$\boldsymbol{F}_{pc}^{\text{isentropic}} = L_{pc}P_c\boldsymbol{N}_{pc},$$
$$\boldsymbol{F}_{pc}^{\text{viscous}} = \boldsymbol{F}_{pc} - L_{pc}P_c\boldsymbol{N}_{pc}.$$

The isentropic part provides the isentropic work of the pressure since

$$\sum_{p\in\mathcal{P}(c)} \boldsymbol{F}_{pc}^{\text{isentropic}}\cdot\boldsymbol{U}_p = P_c V_c (\nabla\cdot U)_c.$$

The viscous part is determined with the help of the entropy inequality. The substitution of the previous decomposition into Eq. (31) leads to

$$m_c T_c \frac{d\sigma_c}{dt} = -\sum_{p\in\mathcal{P}(c)} \boldsymbol{F}_{pc}^{\text{viscous}}\cdot(\boldsymbol{U}_p - \boldsymbol{U}_c). \tag{34}$$

To satisfy a local entropy inequality, the right-hand side of this equation must be positive. Therefore, we postulate the following constitutive relationship to construct the viscous sub-cell force

$$\boldsymbol{F}_{pc}^{\text{viscous}} = -\mathsf{D}_{pc}(\boldsymbol{U}_p - \boldsymbol{U}_c), \tag{35}$$

where D_{pc} is an arbitrary 2×2 positive matrix. This matrix is very important because it directly governs the entropy production, namely the numerical dissipation inherent to the scheme. The phenomenological formula (35) is the most general linear form that we can use to model the viscous sub-cell force. This approach is analogous to the one used in non-equilibrium thermodynamics to establish relation between fluxes and forces [16]. Eq. (35) is a constitutive relation because it links the pressure forces and the velocity jump as follows:

$$-\mathsf{D}_{pc}(\boldsymbol{U}_p - \boldsymbol{U}_c) = L_{\underline{p}}^c(\Pi_{\underline{p}}^c - P_c)\boldsymbol{N}_{\underline{p}}^c + L_{\overline{p}}^c(\Pi_{\overline{p}}^c - P_c)\boldsymbol{N}_{\overline{p}}^c.$$

This formula can be viewed as a generic multi-dimensional Riemann problem. Once the matrix D_{pc} is known, the construction of the scheme is achieved by writing that it must ensure momentum and total energy conservation, that is the sub-cell force must satisfy the balance equation

$$\sum_{p\in\mathcal{P}(c)} L_{pc}P_c\boldsymbol{N}_{pc} - \mathsf{D}_{pc}(\boldsymbol{U}_p - \boldsymbol{U}_c) = 0.$$

This last equation enables us to compute the point velocity $\boldsymbol{U}_p$ and then deduce the nodal pressures.

We realize that using the sub-cell force formalism it is possible to construct many cell-centered schemes that share good physical properties (conservativity and dissipation). The key point in designing these schemes is to know how to construct the corner matrix D_{pc}. We note that our scheme and the scheme developed in [17] can be recast in this general formalism by setting $\mathsf{D}_{pc} = \mathsf{M}_{pc}$ for our scheme and $\mathsf{D}_{pc} = \mathbb{M}_{pc}$ for the Després–Mazeran scheme.

4. The acoustic GRP high-order extension

Concerning the high-order extension, many methods are available. For instance, one can perform a monotone piecewise linear reconstruction for the pressure and the velocity using a slope limiter, followed by the solution of the Riemann problem at nodes with the help of the nodal solver in which we employ the nodal extrapolated values of the pressure and the velocity.

The time discretization is based on a two-steps Runge-Kutta procedure. Such a methodology has been successfully developed in [30,31]. However, this approach is rather expensive since it needs a two-step integration in time. This point becomes particularly crucial when coupling the hydrodynamic scheme with more complex physics. For this reason, we prefer to use a one-step time integrator based on the so-called GRP (Generalized Riemann problem) method of Ben-Artzi and Falcovitz [5,6,4,7,26]. This methodology consists in solving the higher-order Riemann problem with piecewise linear polynomials, whereby the approximate solution is given as a time power series expansion right at the interface, thus providing a numerical flux for a high-order Godunov-type method. We focus on the acoustic approximation of the GRP method. This approximation provides a framework in which the solution of the GRP is simple to compute and easy to handle. In the case of one-dimensional Lagrangian hydrodynamics, this method has been completely derived in the monograph [7]. We recall it briefly for sake of completeness. Then, we present the non-trivial extension of the acoustic GRP methodology to our two-dimensional Lagrangian scheme.

4.1. The one-dimensional case

We recall the GRP methodology in the acoustic approximation for the one-dimensional Euler equations written in the Lagrangian framework

$$\rho \frac{d}{dt}\left(\frac{1}{\rho}\right) - \frac{\partial u}{\partial X} = 0, \tag{36a}$$

$$\rho \frac{du}{dt} + \frac{\partial P}{\partial X} = 0, \tag{36b}$$

$$\rho \frac{dE}{dt} + \frac{\partial}{\partial X}(Pu) = 0. \tag{36c}$$

Here, $\frac{d}{dt}$ is the material derivative and X denotes the Eulerian coordinate at time $t > 0$ whose initial position is x. Its trajectory is given by the kinematic equation

$$\frac{dX}{dt} = u, \quad X(0) = x.$$

In order to mimic what has been done in the two-dimensional case, we discretize the previous equations over the moving cell $\Omega_i(t) = \left[X_{i-\frac{1}{2}}(t), X_{i+\frac{1}{2}}(t)\right]$. Let $\left(\frac{1}{\rho_i^n}, u_i^n, E_i^n\right)$ be the mass average values of $\left(\frac{1}{\rho}, u, E\right)$ over the cell $\Omega_i^n = \left[X_{i-\frac{1}{2}}^n, X_{i+\frac{1}{2}}^n\right]$ at time $t = t^n$. We denote by $\Delta t = t^{n+1} - t^n$ the time increment and assume that the pressure and the velocity at time t^n are piecewise linear, that is for $X \in \left[X_{i-\frac{1}{2}}^n, X_{i+\frac{1}{2}}^n\right]$ and $X_i^n = \frac{1}{2}\left(X_{i-\frac{1}{2}}^n + X_{i+\frac{1}{2}}^n\right)$

$$u(X, t^n) = u_i^n + \delta u_i^n (X - X_i^n),$$
$$P(X, t^n) = P_i^n + \delta P_i^n (X - X_i^n),$$

where δu_i^n and δP_i^n denote the slopes.

The generic high-order Godunov-type scheme takes the form

$$m_i \left(\frac{1}{\rho_i^{n+1}} - \frac{1}{\rho_i^n}\right) - \Delta t\left(u_{i+\frac{1}{2}}^{n+\frac{1}{2}} - u_{i-\frac{1}{2}}^{n+\frac{1}{2}}\right) = 0, \tag{37a}$$

$$m_i(u_i^{n+1} - u_i^n) + \Delta t\left(P_{i+\frac{1}{2}}^{n+\frac{1}{2}} - P_{i-\frac{1}{2}}^{n+\frac{1}{2}}\right) = 0, \tag{37b}$$

$$m_i(E_i^{n+1} - E_i^n) + \Delta t\left[(Pu)_{i+\frac{1}{2}}^{n+\frac{1}{2}} - (Pu)_{i-\frac{1}{2}}^{n+\frac{1}{2}}\right] = 0. \tag{37c}$$

This system is completed by the discrete trajectory equation

$$X_{i+\frac{1}{2}}^{n+1} = X_{i+\frac{1}{2}}^n + \Delta t u_{i+\frac{1}{2}}^{n+\frac{1}{2}}$$

in order to move the mesh.

Here, $u_{i+\frac{1}{2}}^{n+\frac{1}{2}}$, $P_{i+\frac{1}{2}}^{n+\frac{1}{2}}$ and $(Pu)_{i+\frac{1}{2}}^{n+\frac{1}{2}}$ are the fluxes at node $X_{i+\frac{1}{2}}$ averaged over the time interval $[t^n, t^{n+1}]$. The GRP scheme proceeds to derive these mid-point value analytically by resolving the generalized Riemann problem at each point $(X_{i+\frac{1}{2}}^n, t^n)$ with a high-order accuracy. These fluxes are calculated approximately

$$u_{i+\frac{1}{2}}^{n+\frac{1}{2}} = u_{i+\frac{1}{2}}^n + \frac{\Delta t}{2}\left(\frac{du}{dt}\right)_{i+\frac{1}{2}}^n,$$

$$P_{i+\frac{1}{2}}^{n+\frac{1}{2}} = P_{i+\frac{1}{2}}^n + \frac{\Delta t}{2}\left(\frac{dP}{dt}\right)_{i+\frac{1}{2}}^n.$$

The total energy flux is deduced from the previous formulae by setting $(Pu)_{i+\frac{1}{2}}^{n+\frac{1}{2}} = P_{i+\frac{1}{2}}^{n+\frac{1}{2}} u_{i+\frac{1}{2}}^{n+\frac{1}{2}}$.

In the previous formulae, $u^n_{i+\frac{1}{2}}$ and $P^n_{i+\frac{1}{2}}$ are obtained by solving a classical Riemann problem at the interface $X^n_{i+\frac{1}{2}}$ using the extrapolated values of the pressure and the velocity computed from their piecewise linear profiles on each side of the interface.

We can see that once a Riemann solver has been chosen, the GRP scheme is just to obtain the time derivatives $\frac{\partial u}{\partial t})^n_{i+\frac{1}{2}}$, $\frac{\partial P}{\partial t})^n_{i+\frac{1}{2}}$. To compute these time derivatives one has to solve the generalized Riemann problem for system (36) subject to the piecewise linear initial data

$$\mathbf{\Phi}(X,0) = \begin{array}{ll} \mathbf{\Phi}_L + \boldsymbol{\delta}\mathbf{\Phi}_L X & \text{if } X<0, \\ \mathbf{\Phi}_R + \boldsymbol{\delta}\mathbf{\Phi}_R X & \text{if } X>0 \end{array} \tag{38}$$

for $\mathbf{\Phi} = \left(\frac{1}{\rho}, u, E\right)$. The associated Riemann problem is the initial value problem for (36) with the piecewise constant values $\mathbf{\Phi}_L$ and $\mathbf{\Phi}_R$ (zero slopes in (38)). Following [7], the associated Riemann solution is denoted $\boldsymbol{R}^A(X/t, \mathbf{\Phi}_L, \mathbf{\Phi}_R)$. It can be obtained approximately or exactly. The initial structure of the solution $\mathbf{\Phi}(X,t)$ to (36) and (38) is determined by the associated Riemann solution and is described asymptotically as

$$\lim_{t\to 0} \mathbf{\Phi}(\lambda t, t) = R^A(\lambda, \mathbf{\Phi}_L, \mathbf{\Phi}_R), \quad \lambda = X/t. \tag{39}$$

The solution $\mathbf{\Phi}(X,t)$ to the generalized Riemann problem can be represented by an asymptotic expansion in terms of X and t whose zero-order term is given by Eq. (39). To compute the time derivatives, it is sufficient to evaluate the first-order perturbation built into $\mathbf{\Phi}(X,t)$ that is to evaluate

$$\left(\frac{dP}{dt}\right)^\star = \lim_{t\to 0} \frac{d}{dt} P(0,t), \quad \left(\frac{du}{dt}\right)^\star = \lim_{t\to 0} \frac{d}{dt} u(0,t).$$

This problem, which corresponds to the linear GRP, is completely solved in the monograph [7].

For our application, instead of dealing with the general problem, we specialize to the acoustic case which is by far more simple. This particular case is exposed in [7,26], we recall it not only for sake of completeness but also because we will use it extensively to construct the two-dimensional high-order extension. Let us assume that the initial flow variables are all continuous at $X = 0$ so that $\mathbf{\Phi}_L = \mathbf{\Phi}_R$, but we allow jumps in their slopes $\boldsymbol{\delta}\mathbf{\Phi}_L \neq \boldsymbol{\delta}\mathbf{\Phi}_R$. Hence, the GRP solution is continuous at $X = t = 0$. The waves emanating from the origin are just the characteristics curves

$$\mathcal{C}^- : \frac{dX}{dt} = -a, \quad \mathcal{C}^0 : \frac{dX}{dt} = 0, \quad \mathcal{C}^+ : \frac{dX}{dt} = a,$$

where a is the isentropic sound speed. These curves are displayed in Fig. 6. It is shown in [7] that u,P and their derivatives are continuous not only across the contact discontinuity (characteristic $\mathcal{C}^0$) but also across the characteristics $\mathcal{C}^\pm$. Therefore, writing the continuity of the derivative of P along $\mathcal{C}^\pm$, i.e. $\frac{dP}{dt})_{\mathcal{C}^\pm} = \frac{dP}{dt} \pm a\frac{\partial P}{\partial X}$, for $t \to 0$ one gets

$$\left(\frac{dP}{dt}\right)^\star - a_L\left(\frac{\partial P}{\partial X}\right)^\star = \left(\frac{dP}{dt}\right)_L - a_L\left(\frac{\partial P}{\partial X}\right)_L, \quad \text{across } \mathcal{C}^-$$

$$\left(\frac{dP}{dt}\right)^\star + a_R\left(\frac{\partial P}{\partial X}\right)^\star = \left(\frac{dP}{dt}\right)_R + a_R\left(\frac{\partial P}{\partial X}\right)_R, \quad \text{across } \mathcal{C}^+.$$

Here, we have used the chain rule and express the derivative in two ways, approaching the characteristic from either side. We have kept the two-sided notation (such as a_L, a_R, which are all equal) in the previous equations so that we can use them in the numerical applications where $\mathbf{\Phi}_L \neq \mathbf{\Phi}_R$ but $\|\mathbf{\Phi}_L - \mathbf{\Phi}_R\| \ll 1$. Knowing that the flow is isentropic, i.e. $dP = a^2 d\rho$, Eq. (36a) is rewritten

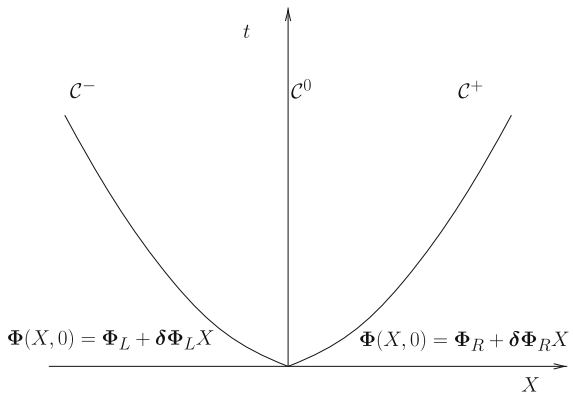

Fig. 6. Characteristic curves in the acoustic case $\mathbf{\Phi}_L = \mathbf{\Phi}_R$, $\boldsymbol{\delta}\mathbf{\Phi}_L \neq \boldsymbol{\delta}\mathbf{\Phi}_R$.

$$\frac{dP}{dt} + \rho a^2 \frac{\partial u}{\partial X} = 0. \tag{40}$$

We express $\frac{\partial P}{\partial X})^\star$ using Eq. (36b). Hence, $\frac{\partial P}{\partial X})^\star = -\rho_L \frac{du}{dt})^\star$ between $\mathcal{C}^-$ and $\mathcal{C}^0$ and $\frac{\partial P}{\partial X})^\star = -\rho_R \frac{du}{dt})^\star$ between $\mathcal{C}^0$ and $\mathcal{C}^+$. The time derivatives $\frac{dP}{dt})_L$ and $\frac{dP}{dt})_R$ are obtained with the help of Eq. (40). Replacing the spatial derivatives of pressure and velocity by the corresponding slopes, one gets

$$\left(\frac{dP}{dt}\right)^\star + \rho_L a_L \left(\frac{du}{dt}\right)^\star = -a_L(\delta P_L + \rho_L a_L \delta u_L), \tag{41a}$$

$$\left(\frac{dP}{dt}\right)^\star - \rho_R a_R \left(\frac{du}{dt}\right)^\star = a_R(\delta P_R - \rho_R a_R \delta u_R). \tag{41b}$$

Finally, the time derivatives for pressure and velocity at contact discontinuity satisfy a 2×2 linear system whose determinant is always strictly positive. Its unique solution is written

$$\left(\frac{dP}{dt}\right)^\star = \frac{a_R(\delta P_R - Z_R \delta u_R) Z_L - a_L(\delta P_L + Z_L \delta u_L) Z_R}{Z_L + Z_R}, \tag{42a}$$

$$\left(\frac{du}{dt}\right)^\star = -\frac{a_L(\delta P_L + Z_L \delta u_L) + a_R(\delta P_R - Z_R \delta u_R)}{Z_L + Z_R}, \tag{42b}$$

where $Z = \rho a$ is the acoustic impedance. We notice that no information concerning the equation of state is needed for the time derivatives computation, therefore this methodology can be also used when dealing with tabulated equation of state.

Now, we are in position to give a summary of our acoustic GRP method applied to the one-dimensional Lagrangian hydrodynamics.

Step 0. Construct a piecewise linear representation of the velocity field and the pressure at time t^n over the cell Ω_i^n

$$u_i^n(X) = u_i^n + \delta u_i^n (X - X_i^n), \quad P_i^n(X) = P_i^n + \delta P_i^n (X - X_i^n).$$

This piecewise linear reconstruction can be computed using a least squares procedure [28]. The advantage of such a procedure is that linear fields are preserved, even for irregular mesh. We shall introduce a classical limitation procedure for the slope in order to achieve a monotonic piecewise linear reconstruction.

Step 1. Given the piecewise linear pressure and velocity at time t^n over the cell Ω_i^n, we solve the Riemann problem for (36) at each grid point $X_{i+\frac{1}{2}}^n$ to define the Riemann solution

$$u_{i+\frac{1}{2}}^n = \frac{Z_i^n u_i^n\left(X_{i+\frac{1}{2}}^n\right) + Z_{i+1}^n u_{i+1}^n\left(X_{i+\frac{1}{2}}^n\right)}{Z_i^n + Z_{i+1}^n} - \frac{P_{i+1}^n\left(X_{i+\frac{1}{2}}^n\right) - P_i^n\left(X_{i+\frac{1}{2}}^n\right)}{Z_i^n + Z_{i+1}^n},$$

$$P_{i+\frac{1}{2}}^n = \frac{Z_i^n P_{i+1}^n\left(X_{i+\frac{1}{2}}^n\right) + Z_{i+1}^n P_i^n\left(X_{i+\frac{1}{2}}^n\right)}{Z_i^n + Z_{i+1}^n} - \frac{Z_i^n Z_{i+1}^n}{Z_i^n + Z_{i+1}^n}\left[u_{i+1}^n\left(X_{i+\frac{1}{2}}^n\right) - u_i^n\left(X_{i+\frac{1}{2}}^n\right)\right].$$

Here, we have written the solution corresponding to the approximate acoustic Riemann solver.

Step 2. Determine the time derivatives $\frac{du}{dt})_{i+\frac{1}{2}}^n$ and $\frac{dP}{dt})_{i+\frac{1}{2}}^n$ using (42) where the left (resp. right) state corresponds to the cell Ω_i^n (resp. Ω_{i+1}^n), and compute the mid-point values

$$u_{i+\frac{1}{2}}^{n+\frac{1}{2}} = u_{i+\frac{1}{2}}^n + \frac{\Delta t}{2}\left(\frac{du}{dt}\right)_{i+\frac{1}{2}}^n,$$

$$P_{i+\frac{1}{2}}^{n+\frac{1}{2}} = P_{i+\frac{1}{2}}^n + \frac{\Delta t}{2}\left(\frac{dP}{dt}\right)_{i+\frac{1}{2}}^n.$$

Step 3. Evaluate the new cell averages $\left(\frac{1}{\rho_i^{n+1}}, u_i^{n+1}, E_i^{n+1}\right)$ using the updating formulae

$$m_i\left(\frac{1}{\rho_i^{n+1}} - \frac{1}{\rho_i^n}\right) - \Delta t\left(u_{i+\frac{1}{2}}^{n+\frac{1}{2}} - u_{i-\frac{1}{2}}^{n+\frac{1}{2}}\right) = 0,$$

$$m_i(u_i^{n+1} - u_i^n) + \Delta t\left(P_{i+\frac{1}{2}}^{n+\frac{1}{2}} - P_{i-\frac{1}{2}}^{n+\frac{1}{2}}\right) = 0,$$

$$m_i(E_i^{n+1} - E_i^n) + \Delta t\,(Pu)_{i+\frac{1}{2}}^{n+\frac{1}{2}} - (Pu)_{i-\frac{1}{2}}^{n+\frac{1}{2}} = 0$$

and advance the grid with the help of the discrete kinematic equation.

We note that the above algorithm is slightly different from the one proposed in [7] in the sense that we are computing the slopes using a least squares procedure (Step 0), whereas in the original approach the slopes are updated using the time deriv-

atives $\frac{du}{dt}\big)_{i+\frac{1}{2}}^{n}$ and $\frac{dP}{dt}\big)_{i+\frac{1}{2}}^{n}$. This modification does not matter since high-order accuracy is still achieved. It has been done in the perspective of the two-dimensional extension.

4.2. The two-dimensional case

With the previous algorithm in mind, we can develop the two-dimensional extension of the acoustic GRP method in the framework of our two-dimensional cell-centered Lagrangian scheme. First, we give the main algorithm of the high-order discretization. Then, we detail the different steps.

4.2.1. GRP algorithm for the two-dimensional Lagrangian scheme

Let $\left(\frac{1}{\rho_c^n}, \boldsymbol{U}_c^n, E_c^n\right)$ be the mass average values of $\left(\frac{1}{\rho}, \boldsymbol{U}, E\right)$ over the cell Ω_c^n at time $t = t^n$. We describe the GRP algorithm corresponding to the high-order discretization of our two-dimensional Lagrangian scheme. The description follows exactly the same steps as those exposed previously for the one-dimensional scheme.

Step 0. Construct a piecewise monotone linear representation of the velocity field and the pressure over the cell Ω_c^n at time t^n

$$\boldsymbol{U}_c(\boldsymbol{X}) = \boldsymbol{U}_c^n + \nabla \boldsymbol{U}_c \cdot (\boldsymbol{X} - \boldsymbol{X}_c^n),$$
$$P_c(\boldsymbol{X}) = P_c^n + \boldsymbol{\nabla} P_c \cdot (\boldsymbol{X} - \boldsymbol{X}_c^n),$$

where $\boldsymbol{X}_c^n$ denotes the centroid of Ω_c^n, $\nabla \boldsymbol{U}_c$ and $\boldsymbol{\nabla} P_c$ are, respectively, the velocity and the pressure gradient in Ω_c^n.

Step 1. Given the piecewise linear pressure and velocity at time t^n over the cell Ω_c^n, we solve the Riemann problem for the two-dimensional gas dynamic equations at each point p. With the help of the nodal solver previously developed, determine the point velocity $\boldsymbol{U}_p^n$ and the nodal pressures $\Pi_{\underline{p}}^{c,n}$, $\Pi_{\bar{p}}^{c,n}$ as follows:

$$\boldsymbol{U}_p^n = (\mathsf{M}_p^n)^{-1} \sum_{c \in \mathcal{C}(p)} [L_{pc}^n P_c(\boldsymbol{X}_p^n) \boldsymbol{N}_{pc}^n + \mathsf{M}_{pc}^n \boldsymbol{U}_c(\boldsymbol{X}_p^n)],$$
$$P_c(\boldsymbol{X}_p^n) - \Pi_{\underline{p}}^{c,n} = Z_{\underline{p}}^{c,n} [\boldsymbol{U}_p^n - \boldsymbol{U}_c(\boldsymbol{X}_p^n)] \cdot \boldsymbol{N}_{\underline{p}}^{c,n},$$
$$P_c(\boldsymbol{X}_p^n) - \Pi_{\bar{p}}^{c,n} = Z_{\bar{p}}^{c,n} [\boldsymbol{U}_p^n - \boldsymbol{U}_c(\boldsymbol{X}_p^n)] \cdot \boldsymbol{N}_{\bar{p}}^{c,n}.$$

Here, the superscript n is used for geometrical quantities such as lengths and normals to emphasize the fact that they are evaluated at time t^n.

Step 2. Determine the time derivatives $\frac{d\boldsymbol{U}}{dt}\big)_p^n$, $\frac{d\Pi}{dt}\big)_{\underline{p}}^{c,n}$ and $\frac{d\Pi}{dt}\big)_{\bar{p}}^{c,n}$ and compute the mid-point values

$$\boldsymbol{U}_p^{n+\frac{1}{2}} = \boldsymbol{U}_p^n + \frac{\Delta t}{2} \left(\frac{d\boldsymbol{U}}{dt}\right)_p^n, \tag{43a}$$

$$\Pi_{\underline{p}}^{c,n+\frac{1}{2}} = \Pi_{\underline{p}}^{c,n} + \frac{\Delta t}{2} \left(\frac{d\Pi}{dt}\right)_{\underline{p}}^{c,n}, \tag{43b}$$

$$\Pi_{\bar{p}}^{c,n+\frac{1}{2}} = \Pi_{\bar{p}}^{c,n} + \frac{\Delta t}{2} \left(\frac{d\Pi}{dt}\right)_{\bar{p}}^{c,n}. \tag{43c}$$

We note that we have introduced the time derivatives corresponding exactly to the point velocity $\boldsymbol{U}_p$ and the nodal pressures $\Pi_{\underline{p}}^c$, $\Pi_{\bar{p}}^c$ defined by the nodal solver.

Step 3. Compute the motion of the mesh thanks to the discrete kinematic equation

$$\boldsymbol{X}_p^{n+1} - \boldsymbol{X}_p^n = \Delta t \boldsymbol{U}_p^{n+\frac{1}{2}} \tag{44}$$

and update the geometrical quantities. Then, evaluate the new cell averages $\left(\frac{1}{\rho_c^{n+1}}, \boldsymbol{U}_c^{n+1}, E_c^{n+1}\right)$ using the updating formulae

$$m_c \left(\frac{1}{\rho_c^{n+1}} - \frac{1}{\rho_c^n}\right) - \Delta t \sum_{p \in \mathcal{P}(c)} \left(L_{\underline{p}}^{c,n+\frac{1}{2}} \boldsymbol{N}_{\underline{p}}^{c,n+\frac{1}{2}} + L_{\bar{p}}^{c,n+\frac{1}{2}} \boldsymbol{N}_{\bar{p}}^{c,n+\frac{1}{2}}\right) \cdot \boldsymbol{U}_p^{n+\frac{1}{2}} = 0, \tag{45a}$$

$$m_c (\boldsymbol{U}_c^{n+1} - \boldsymbol{U}_c^n) + \Delta t \sum_{p \in \mathcal{P}(c)} \left(L_{\underline{p}}^{c,n} \Pi_{\underline{p}}^{c,n+\frac{1}{2}} \boldsymbol{N}_{\underline{p}}^{c,n} + L_{\bar{p}}^{c,n} \Pi_{\bar{p}}^{c,n+\frac{1}{2}} \boldsymbol{N}_{\bar{p}}^{c,n}\right) = 0, \tag{45b}$$

$$m_c (E_c^{n+1} - E_c^n) + \Delta t \sum_{p \in \mathcal{P}(c)} \left(L_{\underline{p}}^{c,n} \Pi_{\underline{p}}^{c,n+\frac{1}{2}} \boldsymbol{N}_{\underline{p}}^{c} + L_{\bar{p}}^{c} \Pi_{\bar{p}}^{c,n+\frac{1}{2}} \boldsymbol{N}_{\bar{p}}^{c,n}\right) \cdot \boldsymbol{U}_p^{n+\frac{1}{2}} = 0. \tag{45c}$$

We note that the geometrical quantities have been used at time $t^{n+\frac{1}{2}}$ in Eq. (45a) in order to be compatible with the point displacement (44). For the momentum and the total energy equations, we have used the geometrical quantities evaluated at the beginning of the time step in order to rigorously ensure the conservativity of the scheme. We shall detail that later on.

In what follows, we are going to detail the construction of steps 0 and 2.

4.2.2. Piecewise monotonone linear reconstruction

To achieve the piecewise linear monotone reconstruction of the pressure and velocity, we used a classical least squares procedure [2,3], followed by a slope limitation procedure.

Let $W \equiv W(\boldsymbol{X})$ denotes a fluid variable (pressure or velocity components), we assume a linear variation for W in cell c

$$W_c(\boldsymbol{X}) = W_c + \boldsymbol{\nabla} W_c \cdot (\boldsymbol{X} - \boldsymbol{X}_c). \tag{46}$$

Here, W_c is the mean value of W in cell c and $\boldsymbol{\nabla} W_c$ is the gradient of W that we are looking for. We note that $\boldsymbol{X_c} = \frac{1}{V_c} \int_{\Omega_c} \boldsymbol{X}\, dV$ is the cell centroid so that the reconstruction is conservative. The gradient in (46) is computed by imposing that

$$W_c(\boldsymbol{X}_d) = W_d \quad \text{for } d \in \mathcal{C}(c),$$

where $\mathcal{C}(c)$ is the set of the neighboring cells of cell c. This problem is generally over-determined and thus the gradient is obtain by using a least squares procedure. Hence, it is the solution of the following minimization problem:

$$\boldsymbol{\nabla} W_c = \operatorname*{argmin}^{-} \sum_{d \in \mathcal{C}(c)} [W_d - W_c - \boldsymbol{\nabla} W_c \cdot (\boldsymbol{X}_d - \boldsymbol{X}_c)]^2.$$

A straightforward computation shows that this solution is written

$$\boldsymbol{\nabla} W_c = \mathsf{M}_c^{-1} \sum_{d \in \mathcal{C}(c)} (W_d - W_c)(\boldsymbol{X}_{cv} - \boldsymbol{X}_c), \tag{47}$$

where M_c is the 2×2 matrix given by

$$\mathsf{M}_c = \sum_{d \in \mathcal{C}(c)} (\boldsymbol{X}_d - \boldsymbol{X}_c) \otimes (\boldsymbol{X}_d - \boldsymbol{X}_c).$$

We notice that M_c is symmetric positive definite and thus always invertible. The main feature of this least squares procedure is that it is valid for any type of unstructured mesh and moreover it preserves the linear fields. This last point is particularly important in view of computing isentropic compression properly.

To preserve monotonicity, we limit the value that the gradient is allowed to take, using the Barth–Jespersen multi-dimensional extension [3] of the van Leer's classical method. For each cell, we introduce the slope limiter $\phi_c \in [0, 1]$ and the limited reconstructed field

$$W_c^{\lim}(\boldsymbol{X}) = W_c + \phi_c \boldsymbol{\nabla} W_c \cdot (\boldsymbol{X} - \boldsymbol{X}_c), \tag{48}$$

where $\boldsymbol{\nabla} W_c$ denotes the approximate gradient given by (47). The coefficient ϕ_c is determined by enforcing the following local monotonicity criterion

$$W_c^{\min} \leqslant W_c^{\lim}(\boldsymbol{X}) \leqslant W_c^{\max} \quad \forall \boldsymbol{X} \in c. \tag{49}$$

Here, we have set $W_c^{\min} = \min(\min_{d \in \mathcal{C}(c)}, W_c)$ and $W_c^{\max} = \max(\max_{d \in \mathcal{C}(c)}, W_c)$. Since the reconstructed field is linear we note that it is sufficient to enforce the following conditions at any point $p \in \mathcal{P}(c)$

$$W_c^{\min} \leqslant W_c^{\lim}(\boldsymbol{X}_p) \leqslant W_c^{\max}, \tag{50}$$

so that the quantity W in the cell c does not lie outside the range of the average quantities in the neighboring cells. Thanks to this formula, we can define the slope limiter as

$$\phi_c = \min_{p \in \mathcal{P}(c)} \phi_{c,p}$$

knowing that

$$\phi_{c,p} = \begin{cases} \mu\left(\frac{W_c^{\max} - W_c}{W_c(\boldsymbol{X}_p) - W_c}\right) & \text{if } W_c(\boldsymbol{X}_p) - W_c > 0, \\ \mu\left(\frac{W_c^{\min} - W_c}{W_c(\boldsymbol{X}_p) - W_c}\right) & \text{if } W_c(\boldsymbol{X}_p) - W_c < 0, \\ 1 & \text{if } W_c(\boldsymbol{X}_p) - W_c = 0. \end{cases}$$

Here, μ denotes a real function that characterizes the limiter. By setting $\mu(x) = \min(1, x)$ we recover the Barth–Jespersen limiter. We can also define a smoother -in the sense that it is more differentiable- limiter by setting $\mu(x) = \frac{x^2 + 2x}{x^2 + x + 2}$. This limiter has been introduced by Vankatakrishnan [42] in order to improve the convergence towards steady solutions for the Euler equations.

These limiters are known to preserve two-dimensional linear fields provided that the neighboring cells whose cell-means are actually involved in the limiting are chosen in a *good neighborhood*. The characterization of such a neighborhood has been derived by Swartz in [40]. The definition is as follows: one has chosen a good neighborhood for a given central cell if and only if the convex hull of the centroids of its associated neighbors contains that central cell. We make such a choice in performing our limitation.

4.2.3. Computation of the time derivatives $\left(\frac{d\boldsymbol{U}}{dt}\right)_p^n$, $\left(\frac{d\Pi}{dt}\right)_{\underline{p}}^{c,n}$ *and* $\left(\frac{d\Pi}{dt}\right)_{\bar{p}}^{c,n}$

Characteristic equations The first step for computing the time derivatives, consists in writing the characteristic equations for the two-dimensional gas dynamics equations [20]. We recall that by using the nonconservative variables $(P, \boldsymbol{U}, \sigma)$, the gas dynamics equation can be written in nonconservative form

$$\frac{dP}{dt} + \rho a^2 \nabla \cdot \boldsymbol{U} = 0, \tag{51a}$$

$$\frac{d\boldsymbol{U}}{dt} + \frac{1}{\rho}\nabla P = 0, \tag{51b}$$

$$\frac{d\sigma}{dt} = 0, \tag{51c}$$

where σ denotes the specific entropy. Let $\boldsymbol{N} = (N_X, N_Y)^t$ denote a particular vector of $\mathbb{R}^2$. The Jacobian matrix in the direction $\boldsymbol{N}$ related to the previous system is written

$$\mathrm{A}(\boldsymbol{N}) = \begin{pmatrix} 0 & \rho a^2 N_X & \rho a^2 N_Y & 0 \\ \frac{N_X}{\rho} & 0 & 0 & 0 \\ \frac{N_Y}{\rho} & 0 & 0 & 0 \\ 0 & 0 & 0 & 0 \end{pmatrix}.$$

The eigenvalues are easily found to be 0 and $\pm a\|\boldsymbol{N}\|$. Thus, we have two simple eigenvalues, which for $\|\boldsymbol{N}\| = 1$ are $\lambda = \pm a$ associated with acoustic waves, and $\lambda = 0$ of multiplicity 2 associated with the entropy waves. To obtain the characteristic equations in the direction $\boldsymbol{N}$ associated with the acoustic waves, we dot-multiply Eq. (51b) by $\pm\rho a\boldsymbol{N}$ and add it to Eq. (51a) to get

$$\frac{dP}{dt} + a\nabla P \cdot \boldsymbol{N} + \rho a\left(\frac{d\boldsymbol{U}}{dt}\cdot\boldsymbol{N} + a\nabla\cdot\boldsymbol{U}\right) = 0, \quad \text{associated with eigenvalue } a, \tag{52a}$$

$$\frac{dP}{dt} - a\nabla P \cdot \boldsymbol{N} - \rho a\left(\frac{d\boldsymbol{U}}{dt}\cdot\boldsymbol{N} - a\nabla\cdot\boldsymbol{U}\right) = 0, \quad \text{associated with eigenvalue } -a, \tag{52b}$$

where $\boldsymbol{N}$ denotes any unit vector.

Construction of a nodal acoustic GRP solver. The second step consists in solving the acoustic GRP problem in the framework of our nodal solver. At time $t = t^n$, let us consider a point p and assume that the flow variables in the surrounding cells are all continuous at $\boldsymbol{X} = \boldsymbol{X}_p$. The pressure and the velocity are continuous and linear, but we allow jumps in their slopes, that is, their slopes are piecewise constant. Let $\boldsymbol{N}$ denote the unit normal to the interface between cells c and d, see Fig. 7. In what follows, we omit the superscript n related to time in order to simplify the notations. We assume that $\boldsymbol{U}$, P and their derivatives are continuous across the characteristics in the direction $\boldsymbol{N}$ associated with the acoustic waves. The time derivatives are defined by setting

$$\left(\frac{d\boldsymbol{U}}{dt}\right)_p = \lim_{t\to t^n}\frac{d\boldsymbol{U}}{dt}(\boldsymbol{X}_p, t), \tag{53a}$$

$$\left(\frac{d\Pi}{dt}\right)_{\bar{p}}^{c} = \lim_{t\to t^n}\lim_{\eta\to 0}\frac{dP}{dt}(\boldsymbol{X}_p - \eta\boldsymbol{N}, t), \tag{53b}$$

$$\left(\frac{d\Pi}{dt}\right)_{\underline{p}}^{d} = \lim_{t\to t^n}\lim_{\eta\to 0}\frac{dP}{dt}(\boldsymbol{X}_p + \eta\boldsymbol{N}, t), \tag{53c}$$

where $\eta > 0$.

In the vicinity of $\boldsymbol{X}_p$ and for $t \to t^n$, the continuity of the derivative of P, $\frac{dP}{dt} - a\nabla P\cdot\boldsymbol{N}$ (resp. $\frac{dP}{dt} + a\nabla P\cdot\boldsymbol{N}$), across the characteristic in the direction $\boldsymbol{N}$ associated with the eigenvalue $-a$ (resp. a), leads to

$$\left(\frac{d\Pi}{dt}\right)_{\bar{p}}^{c} - a_c(\nabla P)_{\underline{p}}^{c}\cdot\boldsymbol{N} = \left(\frac{dP}{dt}\right)_c - a_c(\nabla P)_c\cdot\boldsymbol{N}, \tag{54a}$$

$$\left(\frac{d\Pi}{dt}\right)_{\underline{p}}^{d} + a_d(\nabla P)_{\underline{p}}^{d}\cdot\boldsymbol{N} = \left(\frac{dP}{dt}\right)_d + a_d(\nabla P)_d\cdot\boldsymbol{N}. \tag{54b}$$

As in the one-dimensional case, we express the derivatives in two ways, approaching the characteristic from either side. Here we have set

$$(\nabla P)_{\bar{p}}^{c} = \lim_{t\to t^n}\lim_{\eta\to 0}\nabla P(\boldsymbol{X}_p - \eta\boldsymbol{N}, t), \quad (\nabla P)_{\underline{p}}^{d} = \lim_{t\to t^n}\lim_{\eta\to 0}\nabla P(\boldsymbol{X}_p + \eta\boldsymbol{N}, t).$$

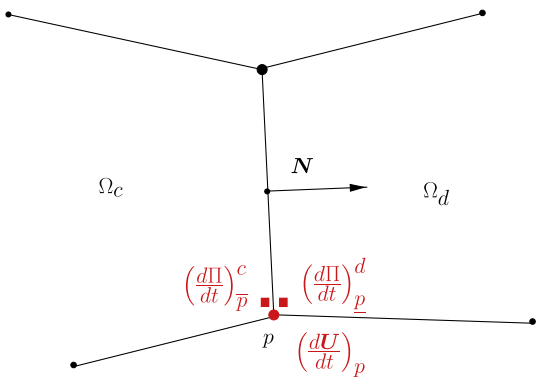

Fig. 7. Generalized Riemann problem at point p.

The other notations are displayed in Fig. 8. With the help of Eq. (51b), we get

$$(\nabla P)^c_{\bar{p}} = -\rho_c \left(\frac{d\boldsymbol{U}}{dt}\right)_p, \quad (\nabla P)^d_{\underline{p}} = -\rho_d \left(\frac{d\boldsymbol{U}}{dt}\right)_p.$$

The time derivatives of pressure in the right-hand side of (54) are expressed thanks to Eq. (51a) and we finally obtain

$$\left(\frac{d\Pi}{dt}\right)^c_{\bar{p}} + Z_c \left(\frac{d\boldsymbol{U}}{dt}\right)_p \cdot \boldsymbol{N} = -a_c[(\nabla P)_c \cdot \boldsymbol{N} + Z_c(\nabla \cdot \boldsymbol{U})_c], \tag{55a}$$

$$\left(\frac{d\Pi}{dt}\right)^d_{\underline{p}} - Z_d \left(\frac{d\boldsymbol{U}}{dt}\right)_p \cdot \boldsymbol{N} = a_d[(\nabla P)_d \cdot \boldsymbol{N} - Z_d(\nabla \cdot \boldsymbol{U})_d]. \tag{55b}$$

In the left-hand sides of the previous equations the velocity divergence and the pressure gradient are computed thanks to the piecewise linear reconstruction. We note the similarity of these equations with those obtained in the one-dimensional case, see system (41). Subtracting (55a) from (55b) we get

$$\left(\frac{d\Pi}{dt}\right)^d_{\underline{p}} - \left(\frac{d\Pi}{dt}\right)^c_{\bar{p}} = (Z_c + Z_d) \left(\frac{d\boldsymbol{U}}{dt}\right)_p \cdot \boldsymbol{N} - \dot{\mathcal{V}}^\star,$$

where $\dot{\mathcal{V}}^\star$ is defined as follows

$$\dot{\mathcal{V}}^\star = -\frac{a_c[(\nabla P)_c \cdot \boldsymbol{N} + Z_c(\nabla \cdot \boldsymbol{U})_c] + a_d[(\nabla P)_d \cdot \boldsymbol{N} - Z_d(\nabla \cdot \boldsymbol{U})_d]}{Z_c + Z_d}.$$

Comparing this result with the time derivative of the velocity obtained solving the one-dimensional acoustic GRP problem, see Eq. (42b), we realize that $\dot{\mathcal{V}}^\star$ can be viewed as the normal component of the one-dimensional solution of the acoustic GRP problem in the direction of the unit normal $\boldsymbol{N}$. Therefore, the time derivatives of the nodal pressures are equal if and only if the projection of the time derivative of the node velocity onto the unit normal is equal to $\dot{\mathcal{V}}^\star$. Since in general $\left(\frac{d\boldsymbol{U}}{dt}\right)_p \cdot \boldsymbol{N} \neq \dot{\mathcal{V}}^\star$, we have the discontinuity $\left(\frac{d\Pi}{dt}\right)^c_{\bar{p}} \neq \left(\frac{d\Pi}{dt}\right)^d_{\underline{p}}$.

Finally, for each face we introduce four time derivatives of the pressure, two for each node on each side of the edges, the discontinuity of these time derivatives across the face implies the loss of momentum and total energy conservation, on the contrary to the one-dimensional case. In what follows, we shall show how to compute these time derivatives by recovering momentum and total energy conservation.

We study momentum conservation by writing the global balance of momentum without taking into account the boundary conditions. The summation of the discrete momentum Eq. (45b) over all the cells leads to

$$\sum_c m_c(\boldsymbol{U}_c^{n+1} - \boldsymbol{U}_c^n) = -\Delta t \sum_c \sum_{p\in\mathcal{P}(c)} (L^{c,n}_{\underline{p}} \Pi^{c,n}_{\underline{p}} \boldsymbol{N}^{c,n}_{\underline{p}} + L^{c,n}_{\bar{p}} \Pi^{c,n}_{\bar{p}} \boldsymbol{N}^{c,n}_{\bar{p}}) - \frac{(\Delta t)^2}{2} \sum_c \sum_{p\in\mathcal{P}(c)} L^{c,n}_{\underline{p}} \left(\frac{d\Pi}{dt}\right)^{c,n}_{\underline{p}} \boldsymbol{N}^{c,n}_{\underline{p}} + L^{c,n}_{\bar{p}} \left(\frac{d\Pi}{dt}\right)^{c,n}_{\bar{p}} \boldsymbol{N}^{c,n}_{\bar{p}}.$$

Here, we have expressed the nodal pressures $\Pi^{c,n+\frac{1}{2}}_{\underline{p}}$, $\Pi^{c,n+\frac{1}{2}}_{\bar{p}}$ thanks to the the Taylor expansions (43b) and (43c). Switching the summation over cells and the summation over nodes in the right-hand side of the previous equation, we get

$$\sum_c m_c(\boldsymbol{U}_c^{n+1} - \boldsymbol{U}_c^n) = -\Delta t \sum_p \sum_{c\in\mathcal{C}(p)} (L^{c,n}_{\underline{p}} \Pi^{c,n}_{\underline{p}} \boldsymbol{N}^{c,n}_{\underline{p}} + L^{c,n}_{\bar{p}} \Pi^{c,n}_{\bar{p}} \boldsymbol{N}^{c,n}_{\bar{p}}) - \frac{(\Delta t)^2}{2} \sum_p \sum_{c\in\mathcal{C}(p)} L^{c,n}_{\underline{p}} \left(\frac{d\Pi}{dt}\right)^{c,n}_{\underline{p}} \boldsymbol{N}^{c,n}_{\underline{p}} + L^{c,n}_{\bar{p}} \left(\frac{d\Pi}{dt}\right)^{c,n}_{\bar{p}} \boldsymbol{N}^{c,n}_{\bar{p}}.$$

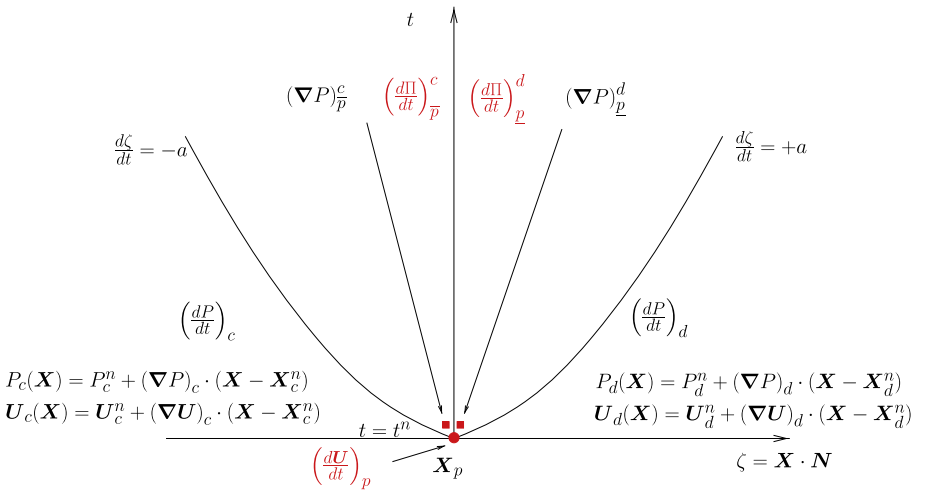

Fig. 8. Structure of the Generalized Riemann problem at point p in the direction of the unit normal $\boldsymbol{N}$. Note that $\zeta = \mathrm{X} \cdot \mathrm{N}$ is the variable in the direction of $\boldsymbol{N}$.

By construction of the classical nodal solver, the term between parentheses in the right-hand side cancels. Then, momentum conservation at the discrete level is ensured, provided that the term between brackets in the right-hand side cancels. Therefore, we deduce the following sufficient condition to ensure discrete momentum conservation

$$\sum_{c \in \mathcal{C}(p)} L_{\underline{p}}^{c,n} \left(\frac{d\Pi}{dt}\right)_{\underline{p}}^{c,n} \boldsymbol{N}_{\underline{p}}^{c,n} + L_{\bar{p}}^{c,n} \left(\frac{d\Pi}{dt}\right)_{\bar{p}}^{c,n} \boldsymbol{N}_{\bar{p}}^{c,n} = 0. \tag{56}$$

We claim that this condition also allows the conservation of total energy. The proof is left to the reader. We note that condition (56) expresses the balance of the forces per unit time induced by the discontinuity of the time derivatives of the nodal pressures. The times derivatives of the nodal pressures, $\left(\frac{d\Pi}{dt}\right)_{\underline{p}}^{c,n}$ and $\left(\frac{d\Pi}{dt}\right)_{\bar{p}}^{c,n}$ are linked to the time derivative of the point velocity, $\left(\frac{d\boldsymbol{U}}{dt}\right)_p^n$, with the help of the following equations:

$$\left(\frac{d\Pi}{dt}\right)_{\underline{p}}^{c,n} + Z_c^n \left(\frac{d\boldsymbol{U}}{dt}\right)_p^n \cdot \boldsymbol{N}_{\underline{p}}^{c,n} = -a_c^n [(\nabla P)_c \cdot \boldsymbol{N}_{\underline{p}}^{c,n} + Z_c^n (\nabla \cdot \boldsymbol{U})_c], \tag{57a}$$

$$\left(\frac{d\Pi}{dt}\right)_{\bar{p}}^{c,n} + Z_c^n \left(\frac{d\boldsymbol{U}}{dt}\right)_p^n \cdot \boldsymbol{N}_{\bar{p}}^{c,n} = -a_c^n [(\nabla P)_c \cdot \boldsymbol{N}_{\bar{p}}^{c,n} + Z_c^n (\nabla \cdot \boldsymbol{U})_c]. \tag{57b}$$

These equations are obtained writing the continuity of the derivatives of P, $\frac{dP}{dt} - a\nabla P \cdot \boldsymbol{N}_{\underline{p}}^{c,n}$ and $\frac{dP}{dt} - a\nabla P \cdot \boldsymbol{N}_{\bar{p}}^{c,n}$, across the characteristics in the directions $\boldsymbol{N}_{\underline{p}}^{c,n}$ and $\boldsymbol{N}_{\bar{p}}^{c,n}$ associated with the eigenvalue $-a$. Once more, this is done in the vicinity of $\boldsymbol{X}_p$ and for $t \to t^n$ (refer to Fig. 9). We realize that the conjunction of (56) and (57) written for each cell surrounding point p, constitutes a close set of equations that allows to determine the time derivatives. Substituting Eqs. (57a) and (57b) into the sufficient condition (56), one obtains

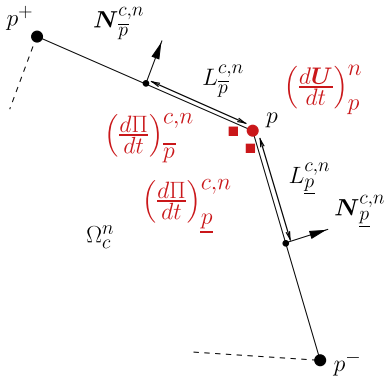

Fig. 9. Localization of the time derivatives of the nodal pressures and velocity at point p viewed from cell Ω_c^n.

$$\mathsf{G}_p\left(\frac{d\boldsymbol{U}}{dt}\right)_p^n = -\sum_{c\in\mathcal{C}(p)} a_c^n[\mathsf{G}_p^c(\nabla P)_c + Z_c^n(L_{\underline{p}}^{c,n}\boldsymbol{N}_{\underline{p}}^{c,n} + L_{\bar{p}}^{c,n}\boldsymbol{N}_{\bar{p}}^{c,n})(\nabla\cdot\boldsymbol{U})_c],$$

where G_p^c and G_p are the 2×2 matrices defined by

$$\mathsf{G}_p^c = Z_c^n[L_{\underline{p}}^{c,n}(\boldsymbol{N}_{\underline{p}}^{c,n}\otimes\boldsymbol{N}_{\underline{p}}^{c,n}) + L_{\bar{p}}^{c,n}(\boldsymbol{N}_{\bar{p}}^{c,n}\otimes\boldsymbol{N}_{\bar{p}}^{c,n})], \quad \mathsf{G}_p = \sum_{c\in\mathcal{C}(p)}\mathsf{G}_p^c.$$

We note that these matrices coincide with the matrices M_p and M_p^c introduced in the nodal solver in the case of the acoustic approximation. Matrices G_p^c and G_p are symmetric positive definite, thus G_p is always invertible and the time derivative of the point velocity is written

$$\left(\frac{d\boldsymbol{U}}{dt}\right)_p^n = -\mathsf{G}_p^{-1}\sum_{c\in\mathcal{C}(p)} a_c^n[\mathsf{G}_p^c(\nabla P)_c + Z_c^n(L_{\underline{p}}^{c,n}\boldsymbol{N}_{\underline{p}}^{c,n} + L_{\bar{p}}^{c,n}\boldsymbol{N}_{\bar{p}}^{c,n})(\nabla\cdot\boldsymbol{U})_c]. \tag{58}$$

The time derivatives of the nodal pressures are deduced from (57).

5. Time step limitation

For numerical applications, the time step is evaluated following two criteria. The first one is a standard CFL criterion which guaranties heuristically the monotone behavior of the entropy. The second is more intuitive, but reveals very useful in practice: we limit the variation of the volume of cells over one time step.

5.1. CFL criterion

We propose a CFL like criterion in order to ensure a positive entropy production in cell c during the time step. At time t_n, for each cell c we denote by λ_c^n the minimal value of the distance between two points of the cell. We define

$$\Delta t_E = C_E \min_c \frac{\lambda_c^n}{a_c^n},$$

where C_E is a strictly positive coefficient and a_c is the sound speed in the cell. The coefficient C_E is computed heuristically and we provide no rigorous analysis which allows such formula. However, extensive numerical experiments show that $C_E = 0.25$ is a value which provides stable numerical results. We have also checked that this value is compatible with a monotone behavior of entropy. The rigorous derivation of this criterion could be obtained by computing the time step which ensures a positive entropy production in cell c from time t^n to t^{n+1}.

5.2. Criterion on the variation of volume

We estimate the volume of the cell c at $t = t^{n+1}$ with the Taylor expansion

$$V_c^{n+1} = V_c^n + \frac{d}{dt}V_c(t^n)\Delta t.$$

Here, the time derivative $\frac{d}{dt}V_c$ is computed by using (10). Let C_V be a strictly positive coefficient, $C_V \in]0,1[$. We look for Δt such that

$$\frac{|V_c^{n+1} - V_c^n|}{V_c^n} \leqslant C_V.$$

To do so, we define

$$\Delta t_V = C_V \min_c \left\{ \frac{V_c^n}{|\frac{d}{dt}V_c(t^n)|} \right\}.$$

For numerical applications, we choose $C_V = 0.1$.

Last, the estimation of the next time step Δt^{n+1} is given by

$$\Delta t^{n+1} = \min(\Delta t_E, \Delta t_V, C_M\Delta t^n), \tag{59}$$

where Δt^n is the current time step and C_M is a multiplicative coefficient which allows the time step to increase. We generally set $C_M = 1.01$.

6. Numerical results

In this section, we present several test cases in order to validate our numerical scheme. For each problem, we use a perfect gas equation of state which is taken to be of the form $P = (\gamma-1)\rho\varepsilon$, where γ is the polytropic index. Most of the computa-

tions have been performed using the Dukowicz approximation for the nodal solver, that is the coefficient Γ_c in the mass swept flux is set equal to $\frac{\gamma+1}{2}$. Each time the acoustic solver will be used, i.e. $\Gamma_c = 0$, it will be explicitly notified.

6.1. Sod problem

This problem is very well known and has been defined in [39]. It consists of a shock tube of unity length. The interface is located at $x = 0.5$. At the initial time, the states on the left and the right sides of $x = 0.5$ are constant. The left state is a high pressure fluid characterized by $(\rho_L, P_L, u_L) = (1, 1, 0)$, the right state is a low pressure fluid defined by $(\rho_R, P_R, u_R) = (0.125, 0.1, 0)$. The gamma gas law is defined by $\gamma = \frac{7}{5}$. The computational domain is defined by $(x, y) \in [0, 1] \times [0, 0.1]$. The initial mesh is a Cartesian grid with 100×2 equally spaced cells. The boundary conditions are wall boundary conditions, that is, the normal velocity is set to zero at each boundary. The numerical results obtained with our GRP acoustic Lagrangian scheme are presented in Fig. 10 as spatial distributions of velocity and density, with the numerical solution plotted as discrete points, and the corresponding exact solution shown as solid lines. Monotonicity is ensured by the Vankatakrishnan limiter. The numerical results show the classical improvement of the high-order solution relative to the first-order one. We also note that our results are very similar to those obtained by Ben-Artzi and Falcovitz in [7].

6.2. Uniformly accelerated piston problem

This test case, taken from [25], describes the compression of a gas, initially at rest, by a uniformly accelerated piston. The piston path is given by $X_p(t) = \frac{1}{2}\kappa t^2$, where $a > 0$. Let ρ_0, P_0 and a_0 denote the constant density, pressure and sound speed of the gas initially located on the right side of the piston. Using the method of characteristics, one can show that this problem admits a smooth isentropic solution up to a critical time t_c which corresponds to the crossings of the characteristics. The critical time writes $t_c = \frac{2}{\gamma+1}\frac{a_0}{\kappa}$ and its corresponding X coordinate is $X_c = \frac{2}{\gamma+1}\frac{a_0^2}{\kappa}$. Knowing this critical time, the analytical solution is written at time $t \in [0, t_c[$ for any $X \in \left[\frac{1}{2}\kappa t^2, a_0 t\right]$

$$a(X,t) = a_0 + \frac{\gamma-1}{2}\kappa\tau(X,t),$$
$$u(X,t) = \kappa\tau(X,t).$$

where $a(X,t)$ denotes the sound speed at time t and coordinate X. Here, the function $\tau(X,t)$ is defined as follows

$$\tau(X,t) = -\frac{\gamma+1}{2\gamma}(t_c - t) + \sqrt{\left(\frac{\gamma+1}{2\gamma}\right)^2 (t_c - t)^2 - \frac{2}{\gamma}\left(\frac{X - a_0 t}{\kappa}\right)}.$$

We note that for $X \geqslant a_0 t$ the solution corresponds to the initial data. Pressure and density are computed using the fact that the flow is isentropic. For numerical applications, we set $\kappa = 0.5$, $\rho_0 = 1$, $P_0 = 1$ and $\gamma = \frac{7}{5}$. Thus, we have $t_c = 1.972$ and $X_c = 2.333$. We have displayed in Fig. 11 snapshots of density for various times ranging from $t = 0.1 t_c$ to $t = 0.99 t_c$. We note the steepening of the density gradient at the head of the density profile, when reaching the critical time. This corresponds to the shock formation. In what follows, we make use of this analytical solution to estimate the global spatial convergence of our first and high-order schemes. For the high-order scheme, we also compare the Barth–Jespersen and the Vankatakrishnan limiter. We briefly describe the methodology used in order to perform the global spatial convergence analysis. The computational domain is the interval [0,2] and the stopping time is $t_s = 1.5$, which is obviously lower than the critical time. For a grid whose mean zone size is Δx, let us denote by $\bar{\varphi}_i^{\Delta x}$ the analytical solution computed at time $t = t_s$ and at the centroid

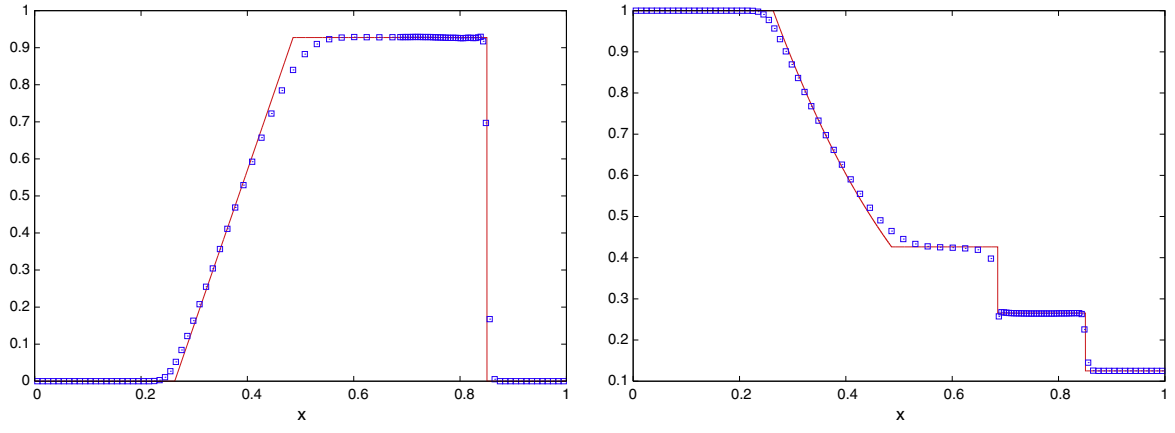

Fig. 10. Solution of the shock tube flow at $t = 0.2$. Numerical versus analytical solution for the velocity (left) and the density (right).

$X_i(t_s)$ of the Lagrangian cell $X_{i-\frac{1}{2}}(t_s), X_{i+\frac{1}{2}}(t_s)$. The numerical solution in this cell is written $\varphi_i^{\Delta x}$. Then, we define for this grid the asymptotic errors using l_1 and l_∞ norms

$$E_{l_1}^{\Delta x} = \sum_{i=1,\ldots,I} |\bar{\varphi}_i^{\Delta x} - \varphi_i^{\Delta x}| \Delta X_i,$$
$$E_{l_\infty}^{\Delta x} = \max_{i=1,\ldots,I} |\bar{\varphi}_i^{\Delta x} - \varphi_i^{\Delta x}|,$$

where I is the total number of cells and ΔX_i is the size of the Lagrangian cell at time t_s. Following Kamm [22], we assume that the asymptotic error for both norms is written

$$E^{\Delta x} = C(\Delta x)^q + O((\Delta x)^{q+1}),$$

where C is the spatial convergence coefficient, and q is the spatial convergence rate. Here, we explicitly assume that the inaccuracy of the solution depends only on the characteristic scale used in the calculation, Δx. We have displayed in Table 1 the results obtained for the density and the velocity using the first-order scheme. We note that the rate of convergence corresponding to the l_1 norm is close to 0.9 whereas the l_∞ convergence rate is close to 0.4. These values are consistent with theory. The results computed with the high-order scheme are displayed in Tables 2 and 3. Table 2 corresponds to Barth–Jespersen limiter and Table 3 to Vankatakrishnan limiter. The l_1 rate of convergence is close to 1.7 for Barth–Jespersen limiter whereas it is close to 1.4 for Vankatakrishnan limiter. In both cases it is greater than 1, hence we get the expected high-order convergence. It turns out that the Vankatakrishnan limiter is more diffusive than the Barth–Jespersen one. We note the discontinuous behavior of the l_∞ rate of convergence which is probably due to the discontinuity of the derivative of the solution at $X = a_0 t$.

6.3. Kidder's isentropic compression

In [24], Kidder has analytically computed the solution of the self-similar isentropic compression of a shell filled with perfect gas. This analytical solution is particularly useful in order to assess the ability of a Lagrangian scheme to properly compute an isentropic compression. More precisely, we want to check that our scheme does not produce spurious entropy during the isentropic compression.

We briefly recall the main features of this solution in order to define the test case. Initially, the shell has the internal (resp. external) radius r_b (resp. r_e). Let P_b, P_e, ρ_b, and ρ_e be the pressures and densities located at r_b and r_e. Since the compression is isentropic, we define $s = \frac{P_e}{\rho_e^\gamma}$, and we have $\rho_b = \rho_e \left(\frac{P_b}{P_e}\right)^{\frac{1}{\gamma}}$. Let $R(r,t)$ be the radius at time $t > 0$ of a fluid particle initially located at radius r. Looking for a solution of the gas dynamics equation under the form $R(r,t) = h(t)r$, using the isentropic feature of the flow and setting $\gamma = 1 + \frac{2}{\nu}$, where $\nu = 1, 2, 3$ indicates planar, cylindrical or spherical symmetry, we finally get the self-similar analytical solution for $t \in [0, \tau[$

$$\rho(R(r,t),t) = h(t)^{-\frac{2}{\gamma-1}} \rho_0 \left[\frac{R(r,t)}{h(t)}\right],$$
$$u(R(r,t),t) = \frac{d}{dt}h(t)\frac{R(r,t)}{h(t)},$$
$$P(R(r,t),t) = h(t)^{-\frac{2\gamma}{\gamma-1}} P_0 \left[\frac{R(r,t)}{h(t)}\right].$$

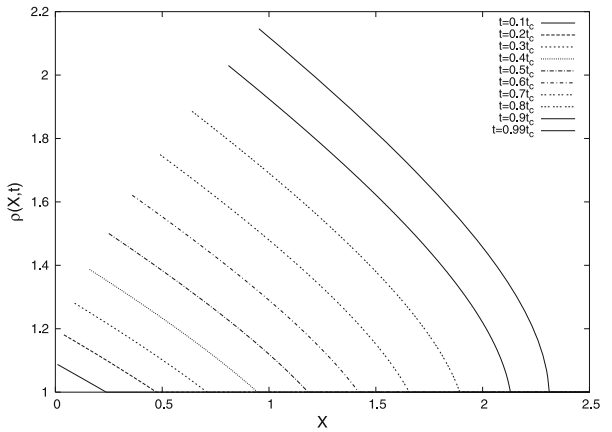

Fig. 11. Analytical solution for the uniformly accelerated piston. Snapshots of density for $t \in [0.1t_c, 0.99t_c]$.

Here, τ denotes the focusing time of the shell which is written

$$\tau = \frac{\gamma-1}{2}\frac{r_e^2 - r_b^2}{a_e^2 - a_b^2},$$

where $a^2 = s\gamma\rho^{\gamma-1}$ is the square of the isentropic sound speed. The particular form of the polytropic index enables us to get the analytical expression $h(t) = 1 - \left(\frac{t}{\tau}\right)^2$, which is valid for any $t \in [0, \tau[$. Note that $h(t)$ goes to zero when t goes to τ, hence τ corresponds to the collapse of the shell on itself. For $r \in [r_b, r_e]$, the initial density and pressure, ρ_0, P_0, are defined by

$$\rho^0(r) = \left(\frac{r_e^2 - r^2}{r_e^2 - r_b^2}\rho_b^{\gamma-1} + \frac{r^2 - r_b^2}{r_e^2 - r_b^2}\rho_e^{\gamma-1}\right)^{\frac{1}{\gamma-1}},$$
$$P^0(r) = s(\rho^0(r))^\gamma.$$

Note that the initial velocity is equal to zero since the shell is assumed to be initially at rest. The isentropic compression is obtained imposing the following pressure laws at the internal and external faces of the shell:

$$P(R(r_b, t), t) = P_b h(t)^{-\frac{2\gamma}{\gamma-1}},$$
$$P(R(r_e, t), t) = P_e h(t)^{-\frac{2\gamma}{\gamma-1}}.$$

We point out that the velocity field is a linear function of the radius R which is a typical property of self-similar isentropic compression.

For numerical applications, we consider a cylindrical shell characterized by $r_b = 0.9$ and $r_e = 1$. We set $P_b = 0.1$, $P_e = 10$, and $\rho_e = 10^{-2}$. Due to cylindrical symmetry we have $\nu = 2$, hence $\gamma = 2$. The previous values enables to get $\rho_b = 2.15 \times 10^{-3}$, $s = 10^5$ and, $\tau = 7.265 \times 10^{-3}$.

The initial computational domain is defined in polar coordinates by $(r, \theta) \in [0.9, 1] \times \left[0, \frac{\pi}{6}\right]$, where $r = \sqrt{x^2 + y^2}$ and $\theta = \arctan\left(\frac{y}{x}\right)$. The computational domain is paved using equally spaced zones in the radial and the angular directions. Kidder's problem is run with the three following polar grids: 25×15, 50×30 and 100×60. The stopping time is chosen to be

Table 1
Convergence analysis related to density and velocity for the uniformly accelerated piston problem computed with the first-order scheme.

Δx	$E_{l_1}^{\Delta x}$	q_{l_1}	$E_{l_\infty}^{\Delta x}$	q_{l_∞}
Density				
0.20E−01	0.11E−01	0.93	0.47E−01	0.45
0.10E−01	0.58E−02	0.92	0.34E−01	0.45
0.50E−02	0.31E−02	0.92	0.25E−01	0.42
0.25E−02	0.16E−02	0.93	0.19E−01	0.44
1.25E−03	0.85E−03	–	0.14E−01	–
Velocity				
0.20E−01	0.98E−02	0.87	0.54E−01	0.44
0.10E−01	0.54E−02	0.90	0.40E−01	0.45
0.50E−02	0.29E−02	0.91	0.29E−01	0.41
0.25E−02	0.15E−02	0.92	0.22E−01	0.43
1.25E−03	0.80E−03	–	0.16E−01	–

Table 2
Convergence analysis related to density and velocity for the uniformly accelerated piston problem computed with the Barth–Jespersen limiter.

Δx	$E_{l_1}^{\Delta x}$	q_{l_1}	$E_{l_\infty}^{\Delta x}$	q_{l_∞}
Density				
0.20E−01	0.32E−03	1.62	0.60E−02	0.24
0.10E−01	0.10E−03	1.88	0.51E−02	1.82
0.50E−02	0.28E−04	1.76	0.14E−02	0.65
0.25E−02	0.83E−05	1.69	0.91E−03	0.66
1.25E−03	0.26E−05	–	0.58E−03	–
Velocity				
0.20E−01	0.36E−03	1.60	0.70E−02	0.23
0.10E−01	0.12E−03	1.88	0.60E−02	1.83
0.50E−02	0.33E−04	1.75	0.17E−02	0.65
0.25E−02	0.97E−05	1.68	0.11E−02	0.66
1.25E−03	0.30E−05	–	0.68E−03	–

Table 3
Convergence analysis related to density and velocity for the uniformly accelerated piston problem computed with the Vankatakrishnan limiter.

Δx	$E_{l_1}^{\Delta x}$	q_{l_1}	$E_{l_\infty}^{\Delta x}$	q_{l_∞}
Density				
0.20E−01	0.64E−03	1.45	0.78E−02	0.15
0.10E−01	0.23E−03	1.46	0.71E−02	1.18
0.50E−02	0.84E−04	1.44	0.31E−02	0.66
0.25E−02	0.31E−04	1.37	0.20E−02	0.68
1.25E−03	0.12E−04	-	0.12E−02	-
Velocity				
0.20E−01	0.71E−03	1.44	0.92E−02	0.14
0.10E−01	0.26E−03	1.44	0.84E−02	1.18
0.50E−02	0.97E−04	1.43	0.37E−02	0.66
0.25E−02	0.36E−04	1.36	0.23E−02	0.68
1.25E−03	0.14E−04	–	0.15E−02	–

very close to the focusing time setting $t_s = 0.99\tau$. The computations are performed with the high-order scheme utilizing the Barth–Jespersen limiter. To estimate precisely the entropy production we define the entropy parameter

$$\alpha = \frac{P}{s\rho^{\gamma}}.$$

We note that for a perfect isentropic compression α is equal to one.

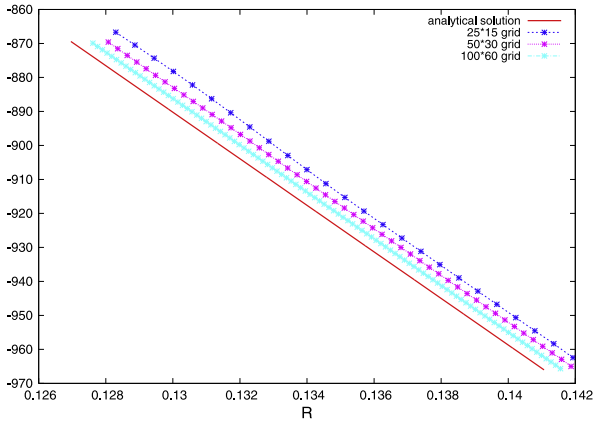

Fig. 12. Kidder's isentropic compression. Radial component of the velocity as function of radius versus analytical solution at stopping time $t_s = 0.99\tau$.

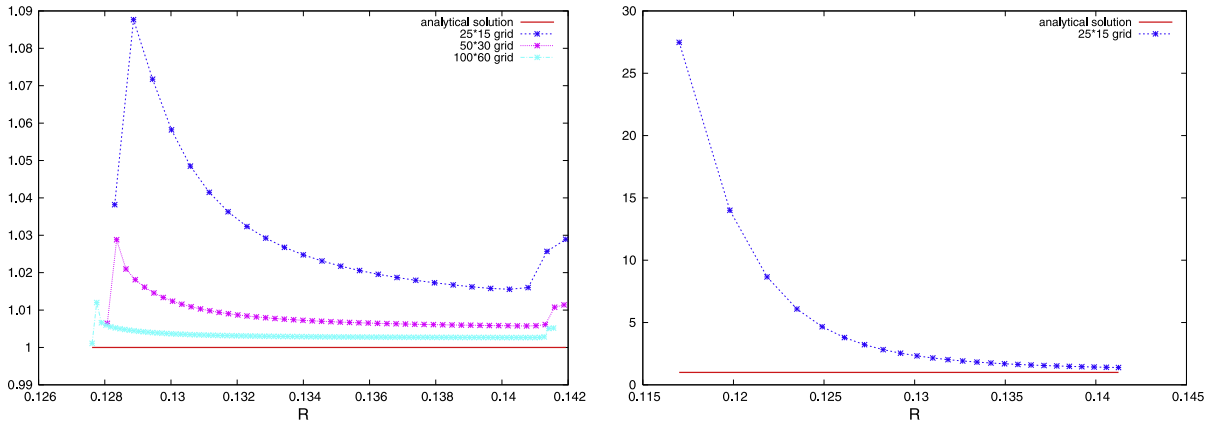

Fig. 13. Kidder's isentropic compression. Entropy parameter as function of radius versus analytical solution at stopping time $t_s = 0.99\tau$. High-order GRP scheme (left) and first-order scheme (right).

We have plotted in Fig. 12 the radial component of the velocity versus the analytical solution at the stopping time. We note that the linear feature of the velocity is very well preserved. We can also see the convergence of the numerical solutions toward the analytical one. In order to evaluate the entropy production, we have displayed in Fig. 13 the entropy parameter respectively for the high-order GRP scheme (left) and for the first-order scheme (right). It turns out that the high-order GRP extension decreases dramatically the value of the entropy parameter and reaches the analytical value. Therefore, we can conclude that our GRP high-order scheme is able to compute properly isentropic compressions. This result comes from the fact that the entropy production within cell Ω_c is proportional to the difference between the point velocity, $\boldsymbol{U}_p$, and the extrapolated value of the velocity field at point p, $\boldsymbol{U}_c(\boldsymbol{X}_p)$. Since, the piecewise linear monotonic reconstruction used in our high-order extension preserves linear fields, it turns out that the entropy production goes to zero. This approach has been used by Christensen [15] in order to design an improved artificial viscosity in the framework of staggered scheme.

6.4. Saltzman problem

This test case taken from [19] is a well known difficult problem that allows to evaluate the robustness of Lagrangian schemes. It consists of a strong piston-driven shock wave calculated using an initially nonuniform mesh. The computational domain is defined by $(x, y) \in [0, 1] \times [0, 0.1]$. The skewed initial mesh, displayed in Fig. 14, is obtained transforming a uniform 100×10 Cartesian grid with the mapping

$$x_{sk} = x + (0.1 - y)\sin(\pi x),$$
$$y_{sk} = y.$$

The initial conditions are $(\rho_0, \varepsilon_0, \boldsymbol{U}_0 = 1, 10^{-6}, 0)$ and the polytropic index is $\gamma = \frac{5}{3}$. At $x = 0$, a unit inward normal velocity is prescribed, the other boundaries are reflective wall. The analytical solution is a one-dimensional infinite strength shock wave that moves at speed $D = \frac{4}{3}$ in the right direction. Thus, the shock wave hits the face $x = 1$ at time $t = 0.75$. Behind the shock, the density is equal to 4. We run this test using the Vankatakrishnan limiter. We have displayed in Fig. 15 the density map and the mesh at time $t = 0.75$ which corresponds to the first bounce of the shock wave. We note that the one-dimensional solution is very well preserved. Moreover, the location of the shock wave and the shock plateau are in good agreement with the analytical solution. In Fig. 16, we have plotted the grid and the density map at time $t = 0.9$ which corresponds to the second bounce. Although the mesh is more wavy than before, it still exhibits a good quality and the computation can be run until time $t = 0.93$. Beyond this time, the computation stops due to too small time steps. These results, in which no spurious modes appear, show the robustness of our high-order GRP scheme.

6.5. Noh problem

The Noh problem [32] is a well known test problem that has been used extensively to validate Lagrangian scheme in the regime of strong shock waves. In this test case, a cold gas with unit density is given an initial inward radial velocity of mag-

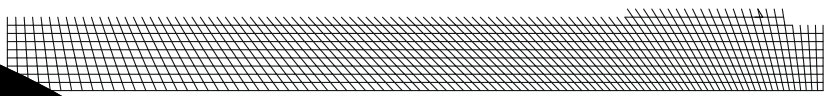

nitude 1. Then, a diverging cylindrical shock wave is generated which propagates at speed $D = \frac{1}{3}$. The density plateau behind the shock wave reaches the value 16. In order to demonstrate the robustness and the accuracy of our GRP scheme, we shall run this test with various options using various types of grids.

6.5.1. One-dimensional Noh problem on polar grids

In this paragraph, we run the Noh problem using polar grids with equi-angular zoning. The initial computational domain is defined in polar coordinates by $(r, \theta) \in [0, 1] \times \left[0, \frac{\pi}{2}\right]$.

First, we address the problem of wave front invariance. This requirement which has been introduced in [10] in the framework of staggered schemes, points out that the artificial viscosity should have no effect along a wave front of constant phase. In the case of our cell-centered scheme, there is no artificial viscosity, however we have to check that the numerical viscosity inherent to our scheme satisfies this wave front invariance requirement. To examine this, we run the Noh problem with two polar grids characterized by the same zoning in the radial direction and two different angular zonings. The density maps at the stopping time $t = 0.6$ are displayed in Fig. 17. We note that the symmetry is perfectly preserved. The shock location and the shock plateau agree with the analytical solution. In Fig. 17, we have plotted the density as function of radius for these two

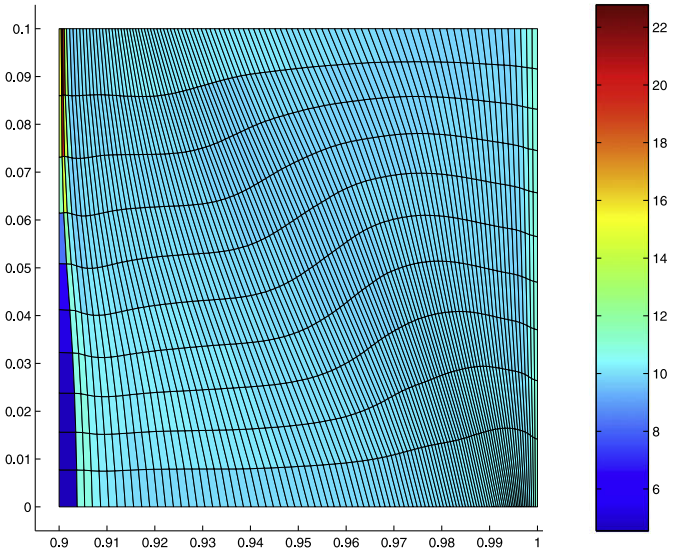

Fig. 16. Mesh and density map for the Saltzman problem at time $t = 0.9$.

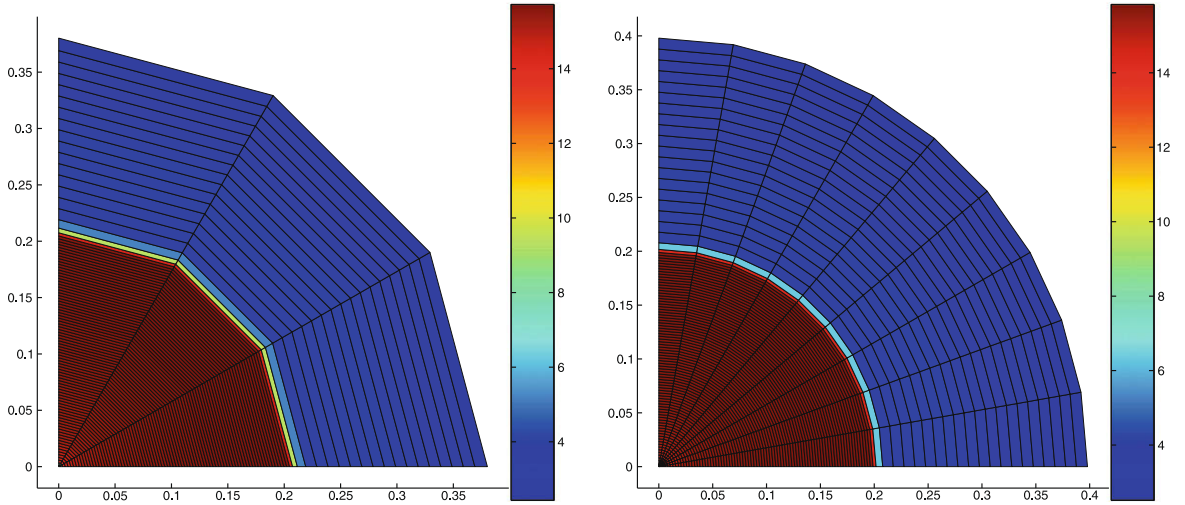

Fig. 17. Mesh and density map for the Noh problem at time $t = 0.6$. The computations are performed with 100 equal radial zones, $\Gamma_c = \frac{\gamma+1}{2}$, and the Vankatakrishnan limiter. The left side computation corresponds to a mesh with 3 equal angular zones whereas the right side one corresponds to a nine equal angular zones mesh.

different angular zonings. The small difference between the two curves shows that the wave front invariance requirement is pretty well satisfied (see Fig. 18). Next, we study the sensitivity of our scheme to the parameter Γ_c which is used to built our approximate solver. We ran computations with a 100×9 polar grid using the Vankatakrishan limiter and two different values of Γ_c, i.e. $\Gamma_c = \frac{\gamma+1}{2}$ and $\Gamma_c = 0$. The latter case corresponds to the acoustic version of our approximate Riemann solver. The densities corresponding to these choices are displayed in Fig. 19 as a function of radius at the stopping time. The shock pla-

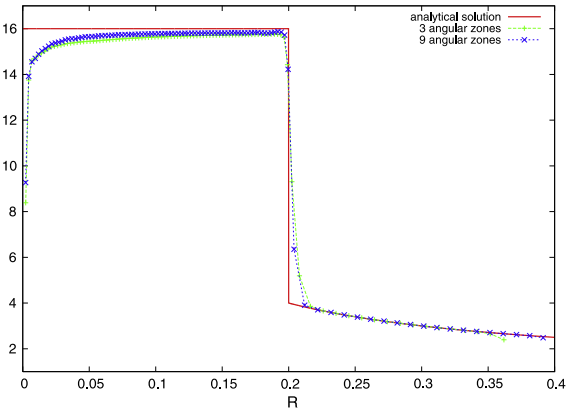

Fig. 18. Density as a function of radius for the Noh problem at stopping time $t = 0.6$. Three equal angular zones computation versus nine equal angular zones computation.

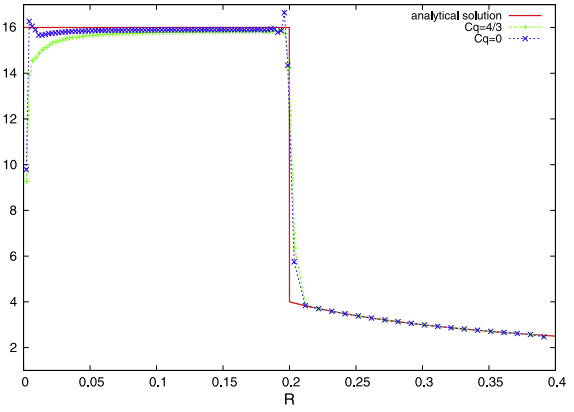

Fig. 19. Density as a function of radius for the Noh problem at stopping time $t = 0.6$. $\Gamma_c = \frac{\gamma+1}{2}$ computation versus $\Gamma_c = 0$ computation.

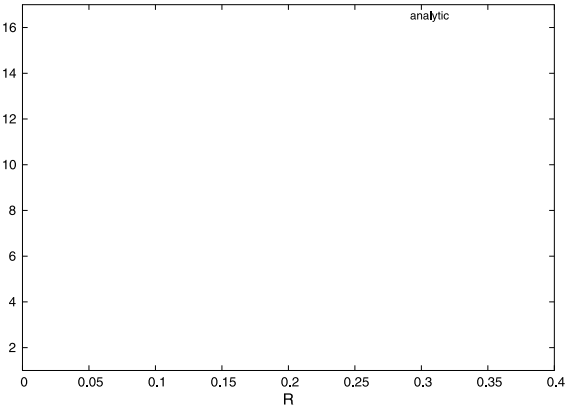

teau and the shock location are almost the same, however in the acoustic case, we note the appearance of density peaks located near the origin and the shock front. This peak occurrence is probably due to the fact that the acoustic formulation does not produce enough dissipation.

Now, we study the sensitivity to the limiters running the Noh problem with a 100×9 polar grid and $\Gamma_c = \frac{\gamma+1}{2}$, using the Barth–Jespersen and the Vankatakrishan limiters. The density versus radius is plotted in Fig. 20 for both computations. We see almost no discrepancy between the two curves. This shows that both limiters acts in the same manner for infinite strength shock waves.

Finally, we assess the convergence of our scheme computing the Noh problem with the three following polar grids: 100×9, 200×9 and 400×9. These computations are run using $\Gamma_c = \frac{\gamma+1}{2}$ and the Vankatakrishnan limiter. We can observe in Fig. 21 the convergence of the numerical solutions toward the analytical one.

6.5.2. Two-dimensional Noh problem on a 50×50 Cartesian grid

In order to assess the robustness of our scheme, we run the Noh problem on a 50×50 Cartesian grid. This configuration leads to a more severe test case since the mesh is not aligned with the flow. The computation is performed using $\Gamma_c = \frac{\gamma+1}{2}$ and the Vankatakrishnan limiter. We have displayed the grid and the density map in Fig. 22. We note that the cylindrical symmetry is quite well preserved and that the shock is located at a circle whose radius is approximately 0.2. The results for this test case are almost as good as those obtained by Campbell and Shashkov [8] using their staggered scheme with a mimetic tensorial artificial viscosity.

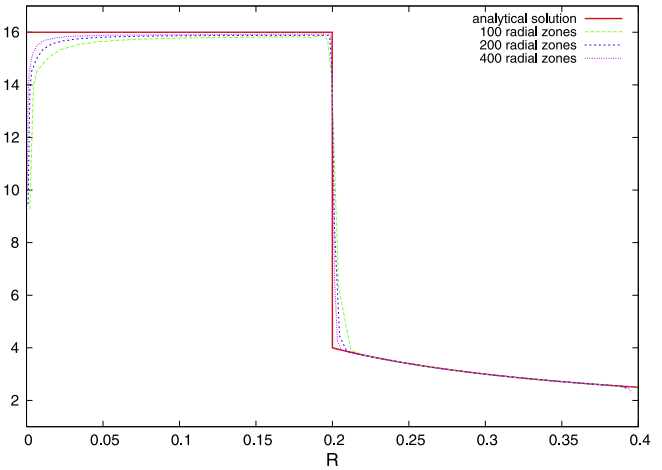

Fig. 21. Density as a function of radius for the Noh problem at stopping time $t = 0.6$. Convergence analysis.

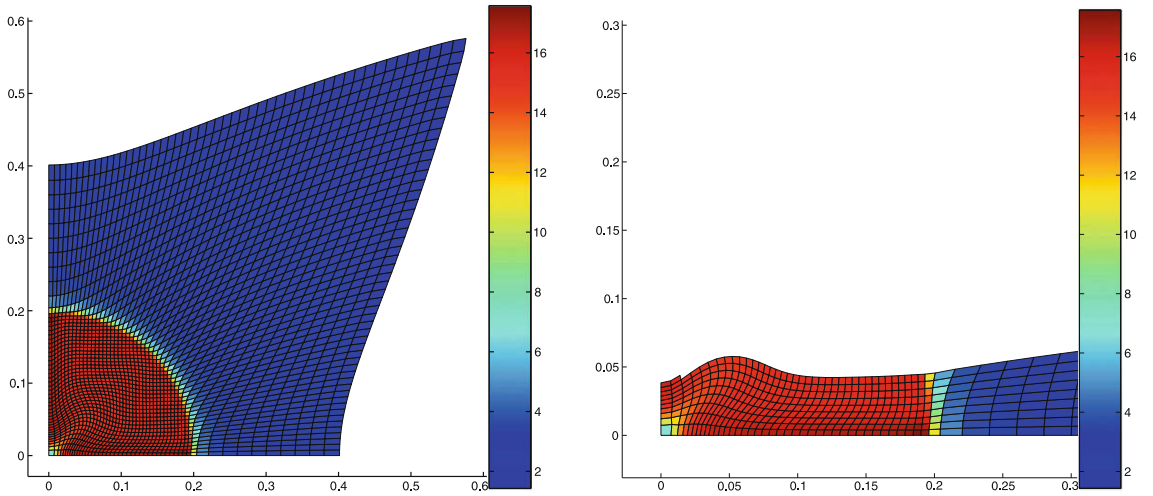

6.5.3. Two-dimensional Noh problem on a non-conformal grid

We finish this section with the computation of the Noh problem on a non-conformal grid in order to illustrate the ability of our scheme to handle unstructured grids. This non-conformal grid is constructed using a polar grid and adding to it one level of refinement, see Fig. 23 (left). Thus, we get a grid made of triangles, quadrangles and pentagons. We put the stress on the fact that no special treatment is required in our solver to handle such a grid. We have displayed the grid at the stopping time $t = 0.6$ in Fig. 23 (right). We point out that the symmetry is well preserved and the shock location agrees with the analytical solution. The density in all the cells as function of radius of the cell centroid is plotted in Fig. 24. The shock location and the shock plateau are in good agreement with the analytical solution. We notice some small overshoots in the density plateau corresponding to the location of the non-conformal cells. These undershoots are probably a consequence of the loss of convexity of the pentagonal interface zones.

6.6. Sedov problem

We consider the Sedov problem for a point-blast in a uniform medium with cylindrical symmetry. An exact solution based on self-similarity arguments is available, see for instance [23]. The initial conditions are characterized by $(\rho_0, P_0, \boldsymbol{U}_0) = (1, 10^{-6}, 0)$ and the polytropic index is set equal to $\frac{7}{5}$. We set an initial delta-function energy source at the origin prescribing the pressure in the cell containing the origin as follows:

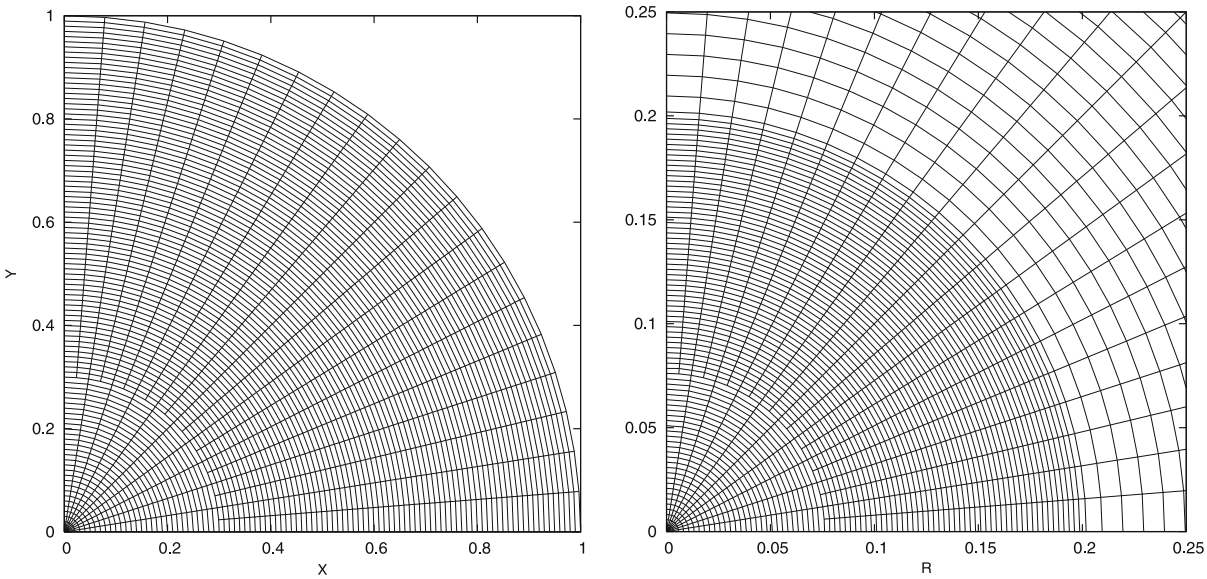

Fig. 23. Noh problem on a non-conformal grid. Initial grid (left) and zoom on the final grid at $t = 0.6$ (left).

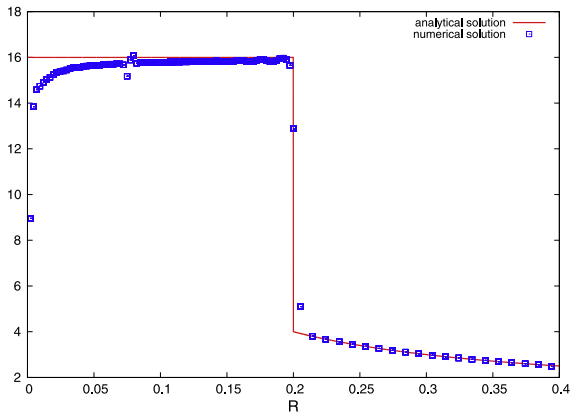

Fig. 24. Noh problem on a non-conformal grid. Density versus cell centroid radius at $t = 0.6$.

$$P_{\text{or}} = (\gamma - 1)\rho_{\text{or}} \frac{\mathcal{E}_0}{V_{\text{or}}},$$

where V_{or} denotes the volume of the cell and $\mathcal{E}_0$ is the total amount of released energy. Choosing $\mathcal{E}_0 = 0.244816$, as it is suggested in [23], the solution consists of a diverging shock whose front is located at radius $R = 1$ at time $t = 1$. The peak density reaches the value 6.

We run a computation with 30×30 equally space zones on the domain $(x, y) \in [0, 1.2] \times [0, 1.2]$. Then, keeping the same conditions, we run the Sedov problem on a polygonal grid produced by a Voronoi tesselation [27]. The numerical results obtained using the Vankatakrishnan limiter are plotted in Fig. 25. We note that our GRP high-order scheme preserves very well the one-dimensional cylindrical symmetry of the solution. As it can be seen in Fig. 26 the shock position is very well resolved without any spurious oscillations.

We have also run the Sedov problem using the same initial conditions on the unstructured grid displayed in Fig. 27 (left). We point out that this grid is made of three structured zones paved with quadrangular cells. The central square zone is meshed with 15×15 cells and the two remaining curvilinear zones are meshed with 45×15 cells. The junction of these three zones is a triple point, that is an exceptional vertex surrounded by three cells. We have displayed in Fig. 28 the density map and the density as function of radius of the cells at $t = 1$ in Fig. 27 (right). Once again, the symmetry of the one-dimensional cylindrical flow is quite well preserved and the shock is very well resolved. We point out that the quality of mesh in the vicinity of the triple point is particularly good as it can be seen in Fig. 28 (right).

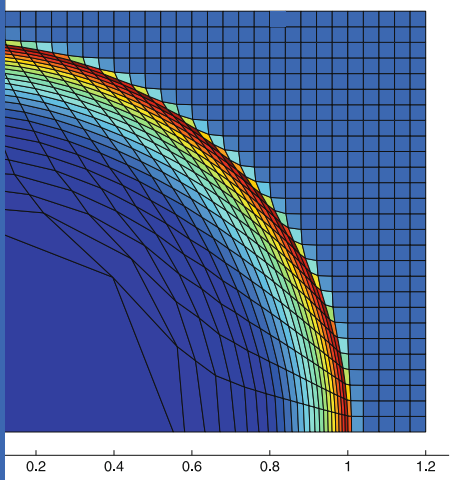

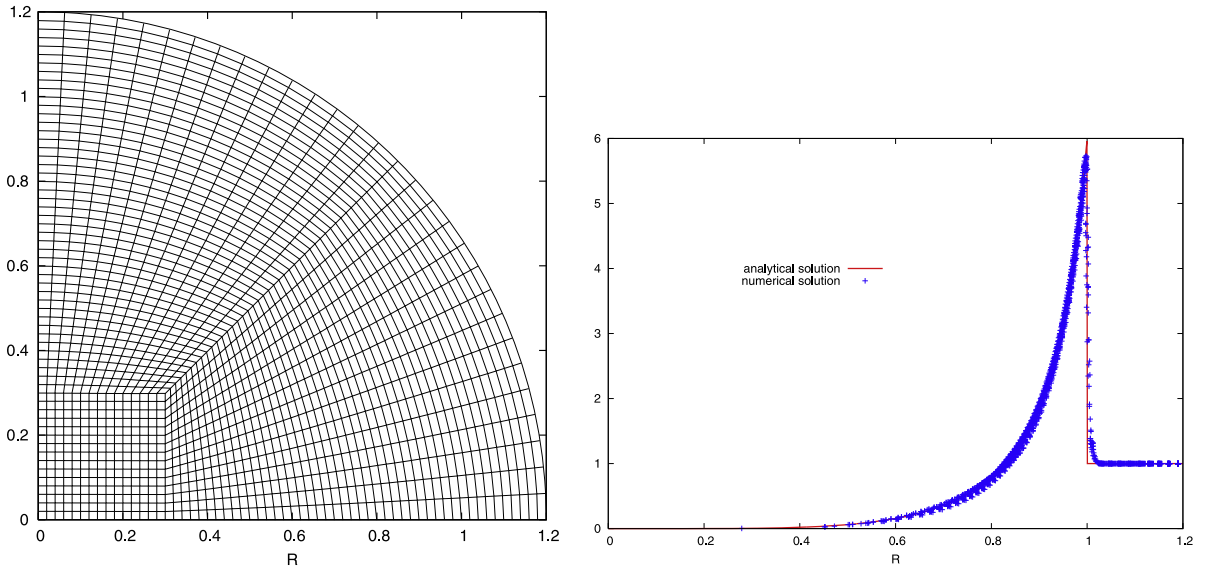

Fig. 27. Initial unstructured grid for the Sedov problem (left). Density as function of radius of the centroid of cell versus analytical solution (right) at stopping time $t = 1$.

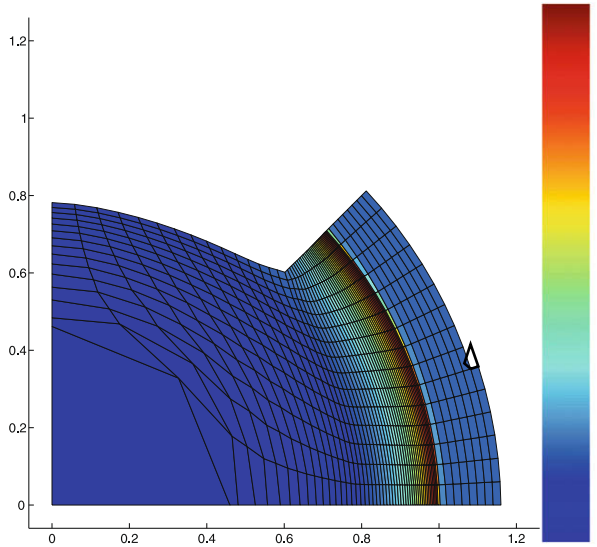

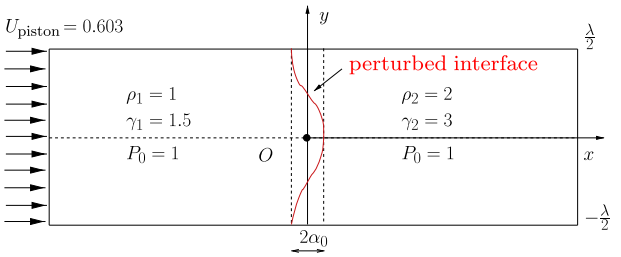

Fig. 29. Shock tube configuration for the shock-contact interaction problem.

6.7. Study of the linear phase of the Richtmyer–Meshkov instability

This test case is devoted to the study of the linear phase of the Richtmyer–Meshkov instability [34] for a piston-driven flow. This hydrodynamic instability occurs when a shock wave hits a perturbed interface separating two different fluids. For sufficiently small perturbations, analytical solutions can be derived using linear perturbation theory [45]. In this framework, the theory shows that the amplitude of the perturbation grows linearly as function of time. We first study the unperturbed fluid configuration in the RMI problem, which is a collision of a shock wave with a flat contact discontinuity. Such a collision produces a transmitted shock wave and a reflected wave that can be either a shock or a rarefaction. This shock-contact interaction defines a one-dimensional Riemann problem, which can be solved analytically.

In what follows, we will employ the configuration displayed in Fig. 29. The interface is located at $x = 0$ and the computational domain corresponding to the shock tube is defined by $(x, y) \in [-5, 4.2] \times [0, 0.5]$, since the $y = 0$ line is a symmetry axis for this problem. For the initial and boundary conditions described in Fig. 29, the incident piston-driven shock hits the interface at time $t = 3.015$. This interaction leads to transmitted and reflected shock waves, which also later interact with the piston and the right boundary wall. The time history of the shock-contact interaction is displayed in Fig. 30 using a classical $(t - x)$ diagram. We run a computation for the unperturbed configuration with our high-order scheme (BJ limiter) using 460 equally-spaced cells in the x direction and one cell in the y direction. The density as function of x coordinate is plotted in Fig. 31 versus analytical solution at time $t = 5$. We point out the very good agreement between numerical and analytical solutions. Moreover, we note that transmitted and reflected shocks are sharply resolved. In order to study the perturbed configuration, we initialize a cosinusoidal perturbation of the interface with a small amplitude α_0. Thus, the equation of the interface is written

$$x(y) = a_0 \cos\left(\frac{2\pi}{\lambda} y\right) \quad \text{for } y \in \left[-\frac{\lambda}{2}, \frac{\lambda}{2}\right], \tag{60}$$

where λ is the wavelength of the perturbation. The shape of the perturbed interface is displayed in Fig. 29. For a small enough initial amplitude, linear theory predicts that the perturbation amplitude, $\alpha(t)$, grows linearly as function of time, after the

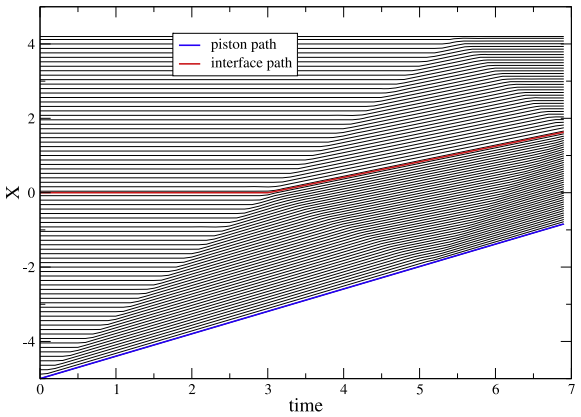

Fig. 30. $t - x$ diagram for the shock-contact interaction problem.

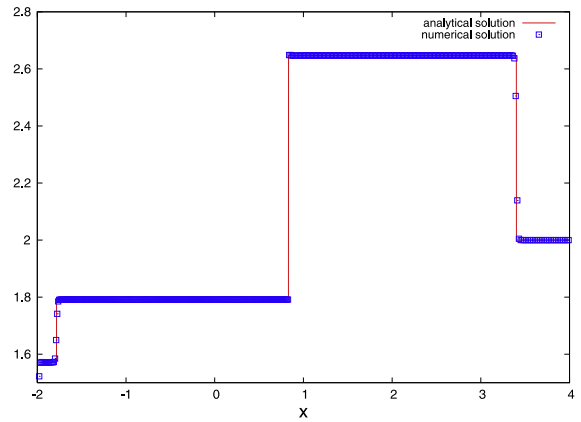

Fig. 31. Interaction of a shock wave with a contact discontinuity. Density as function of X coordinate versus analytical solution at time $t = 5$.

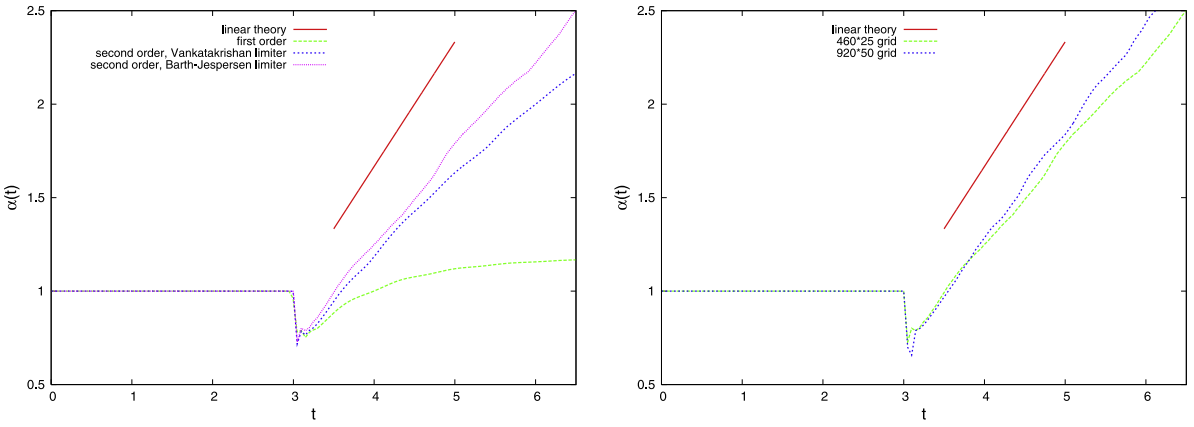

Fig. 32. Shock-contact interaction problem. Numerical perturbation amplitudes as function of time versus linear theory. Comparison between first-order, second-order Barth–Jespersen and Vankatakrishnan for the 460×24 grid (left). Mesh refinement for the second-order Barth–Jespersen computation (right).

shock has interacted with the interface. Using direct two-dimensional simulation of the perturbed configuration, we shall recover this important result and compare the numerical perturbation amplitude with the one coming from the linear theory. The numerical simulations are made meshing the computational domain, $(x,y) \in [-5,4.2] \times [0,0.5]$, with 460×25 equally spaced cells. Hence, we have set $\lambda = 1$ and meshed only a half wavelength due to the symmetry of the problem about x axis. We set $\alpha_0 = 10^{-4}$ and perform three computations utilizing respectively first-order scheme, high-order scheme with Vankatakrishan limiter and high-order scheme with Barth–Jespersen limiter. The perturbed interface is prescribed by moving the vertices initially located on the line $x = 0$ onto the curve defined by Eq. (60). The perturbation amplitude, $\alpha(t)$, is computed using the following formula:

$$\alpha(t) = (X_{\text{pert}}(t) - X_{\text{unpert}}(t))/\alpha_0, \tag{61}$$

where $X_{\text{pert}}(t)$ (resp. $X_{\text{unpert}}(t)$) is the abscissa of a point located on the perturbed (resp. unperturbed) interface. Using this formula for the three previous computations, we compute the corresponding perturbation amplitudes and compare them to the reference one coming from the linear theory [45]. We have plotted in Fig. 32 (left) the numerical perturbation amplitudes as function of time versus the one coming from the linear theory. We remark that the high-order computations recover quite well the linear theory whereas the first-order calculation exhibits a highly damped evolution of the perturbation. This damping is the consequence of the high numerical dissipation inherent to the first-order scheme. Concerning the high-order results, we note that the perturbation amplitude obtained using the Barth–Jespersen limiter is closer to the linear theory curve than the perturbation amplitude obtained using the Vankatakrishnan limiter. This remark comes from the fact that the Vankatakrishnan limiter is more diffusive than the Barth–Jespersen one. We have also performed a computation using a finer grid with 920×50 cells with the Barth–Jespersen limiter. We observe in Fig. 32 (right) that the resulting amplitude perturbation follows the linear theory, i.e the slopes are identical. These results show the ability of our high-order cell-centered Lagrangian scheme to simulate very accurately complex phenomena such as hydrodynamic instabilities.

7. Conclusion

A high-order cell-centered unstructured scheme, based on the generalized Riemann problem methodology, has been presented for solving the compressible Euler equations written in Lagrangian form. Vertex velocity and face fluxes are computed coherently thanks to an approximate Riemann solver located at nodes. In this way, we provide a discretization that fulfills the requirement related to the geometric conservation law. The present discretization leads to a conservative scheme, which, in its first-order version, satisfies a local entropy inequality. The developed method is used to compute a variety of compressible flow problems on arbitrary unstructured grids. The numerical results demonstrated the accuracy and the robustness of this method.

In the future, we intend to improve the nodal approximate Riemann solver, in the sense of better distributing numerical entropy through shock waves, using the sub-cell forces based discretization. Moreover, in a forthcoming paper, we shall derive the cylindrical version of the present scheme, addressing the difficult issue related to the problem of symmetry preservation.

Acknowledgments

We thank B. Nkonga for his interest and many fruitful discussions. We also want to thank O. Cessenat for his valuable help in improving the manuscript.

References

[1] F.L. Adessio, D.E. Carroll, K.K. Dukowicz, J.N. Johnson, B.A. Kashiwa, M.E. Maltrud, H.M. Ruppel. Caveat: a computer code for fluid dynamics problems with large distortion and internal slip, Technical Report LA-10613-MS, Los Alamos National Laboratory, 1986.
[2] T.J. Barth, Numerical methods for conservation laws on structured and unstructured meshes, Technical report, VKI Lecture Series, 2003.
[3] T.J. Barth, D.C. Jespersen, The design and application of upwind schemes on unstructured meshes, in: AIAA paper 89-0366, 27th Aerospace Sciences Meeting, Reno, Nevada, 1989.
[4] M. Ben-Artzi, A. Birman, Application of the generalized Riemann problem method to 1-D compressible flows, J. Comput. Phys. 65 (1986) 170–178.
[5] M. Ben-Artzi, J. Falcovitz, A second-order Godunov-type scheme for compressible fluid dynamics, J. Comput. Phys. 55 (1) (1984) 1–32.
[6] M. Ben-Artzi, J. Falcovitz, An upwind second-order scheme for compressible duct flows, SIAM J. Sci. Stat. Comput. 7 (3) (1986) 744–768.
[7] M. Ben-Artzi, J. Falcovitz, Generalized Riemann Problems in Computational Fluids Dynamics, Cambridge University Press, 2003.
[8] J.C. Campbell, M.J. Shashkov, A tensor artificial viscosity using a mimetic finite difference algorithm, J. Comput. Phys. 172 (4) (2001) 739–765.
[9] J.C. Campbell, M.J. Shashkov, A compatible Lagrangian hydrodynamics algorithm for unstructured grids, Seltuk J. Appl. Math. 4 (2) (2003) 53–70.
[10] E.J. Caramana, M.J. Shashkov, P.P. Whalen, Formulations of artificial viscosity for multidimensional shock wave computations, J. Comput. Phys. 144 (1998) 70–97.
[11] E.J. Caramana, D.E. Burton, M.J. Shashkov, P.P. Whalen, The construction of compatible hydrodynamics algorithms utilizing conservation of total energy, J. Comput. Phys. 146 (1998) 227–262.
[12] E.J. Caramana, M.J. Shashkov, Elimination of artificial grid distortion and hourglass – type motions by means of Lagrangian subzonal masses and pressures, J. Comput. Phys. 142 (1998) 521–561.
[13] G. Carré, S. Delpino, B. Després, E. Labourasse, A cell-centered Lagrangian hydrodynamics scheme in arbitrary dimension, J. Comput. Phys., submitted for publication.
[14] A. Chorin, J. Marsden, A Mathematical Introduction to Fluid Mechanics, Springer-Verlag, 1992.
[15] R.B. Christensen, Godunov methods on a staggered mesh-an improved artificial viscosity, Technical Report UCRL-JC-105269, Lawrence Livermore National Laboratory, 1991.
[16] S.R. de Groot, P. Mazur, Non-equilibrium Thermodynamics, Dover, 1984.
[17] B. Després, C. Mazeran, Lagrangian gas dynamics in two dimensions and Lagrangian systems, Arch. Rational Mech. Anal. 178 (2005) 327–372.
[18] J.K. Dukowicz, A general non-iterative Riemann solver for Godunov's method, J. Comput. Phys. 61 (1984) 119–137.
[19] J.K. Dukowicz, B. Meltz, Vorticity errors in multidimensional Lagrangian codes, J. Comput. Phys. 99 (1992) 115–134.
[20] E. Godlewski, P.A. Raviart, Hyperbolic Systems of Conservation Laws, Springer-Verlag, 2000.
[21] S.K. Godunov, A. Zabrodine, M. Ivanov, A. Kraiko, G. Prokopov, RTsolution numTrique des problFmes multidimensionnels de la dynamique des gaz, Mir, 1979.
[22] J.R. Kamm, W.J. Rider, J.S. Brock, Consistent metrics for code verification, Technical Report LA-UR-02-3794, Los Alamos National Laboratory, 2002.
[23] J.R. Kamm, F.X. Timmes, On efficient generation of numerically robust Sedov solutions, Technical Report LA-UR-07-2849, Los Alamos National Laboratory, 2007.
[24] R.E. Kidder, Laser-driven compression of hollow shells: power requirements ANS stability limitations, Nucl. Fus. 1 (1976) 3–14.
[25] L. Landau, E. Lifchitz, MTcanique des Fluides, Mir, 1989.
[26] J. Li, Z. Sun, Remark on the generalized Riemann problem method for compressible fluid flows, J. Comput. Phys. 222 (2007) 796–808.
[27] R. LoubFre, M.J. Shashkov, A subcell remapping method on staggered polygonal grids for Arbitrary-Lagrangian–Eulerian methods, J. Comput. Phys. 23 (2004) 155–160.
[28] S.M. Murman, M. Berger, M.J. Aftosmis, Analysis of slope limiters on irregular grids, Technical Report NAS-05-007, NAS Technical Report, 2005.
[29] P.H. Maire, R. Abgrall, J. Breil, J. Ovadia, A cell-centered Lagrangian scheme for compressible flow problems, SIAM J. Sci. Comput. 29 (4) (2007) 1781–1824.
[30] P.H. Maire, J. Breil, A second-order cell-centered lagrangian scheme for two-dimensional compressible flow problems, Int. J. Numer. Methods Fluids 56 (2008) 1417–1423.
[31] P.H. Maire, B. Nkonga, Multi-scale Godunov-type method for cell-centered discrete Lagrangian hydrodynamics, J. Comput. Phys., 2008, doi: 10.1016/j.jcp.2008.10012.
[32] W.F. Noh, Errors for calculations of strong shocks using artificial viscosity and an artificial heat flux, J. Comput. Phys. 72 (1987) 78–120.
[33] B. Rebourcet, Comments on the filtering of numerical instabilities in Lagrangian hydrocodes, in: Conference on Numerical methods for multi-material fluid flows; Czech Technical University in Prague on September 10–14, 2007. <http://www-troja.fjfi.cvut.cz/multimat07/presentations/tuesday/Rebourcet_filtering.pdf>.
[34] R.D. Richtmyer, Taylor instability in shock acceleration of compressible fluids, Commun. Pure Appl. Math. 13 (1960) 297–319.
[35] G. Scovazzi, Stabilized shock hydrodynamics: II. Design and physical interpretation of the SUPG operator for Lagrangian computations, Comput. Methods Appl. Mech. Eng. 196 (2007) 966–978.
[36] G. Scovazzi, M.A. Christon, T.J. R Hughes, J.N. Shadid, Stabilized shock hydrodynamics: I. A Lagrangian method, Comput. Methods Appl. Mech. Eng. 196 (2007) 923–966.
[37] G. Scovazzi, E. Love, M.J. Shashkov, Multi-scale Lagrangian shock hydrodynamics on Q1/P0 finite elements: theoretical framework and two-dimensional computations, Comput. Methods Appl. Mech. Eng. 197 (2008) 1056–1079.
[38] M. Shashkov, Conservative Finite Difference Methods on General Grids, CRC Press, 1996.
[39] G.A. Sod, A survey of several finite difference methods for systems of non-linear hyperbolic conservation laws, J. Comput. Phys. 27 (1978) 1–31.
[40] B. Swartz, Good neighborhoods for multidimensional Van Leer limiting, J. Comput. Phys. 154 (1999) 237–241.
[41] B. van Leer, Towards the ultimate conservative difference scheme, J. Comput. Phys. 32 (1979) 101–136.
[42] V. Venkatakrishnan, Convergence to steady state solutions of the Euler equations on unstructured grids with limiters, J. Comput. Phys. 118 (1995) 120–130.
[43] J. von Neumann, R.D. Richtmyer, A method for the numerical calculations of hydrodynamical shocks, J. Appl. Phys. 21 (1950) 232–238.
[44] M.L. Wilkins, Calculation of elastic plastic flow, Methods Comput. Phys. 3 (1964).
[45] Y. Yang, Q. Zhang, D.H. Sharp, Small amplitude theory of Richtmyer–Meshkov instability, Phys. Fluids 6 (5) (1994) 1856–1873.